Determining Excited-State Structures and Photophysical Properties in Phenylphosphine Rhenium(I) Diimine Biscarbonyl Complexes Using Time-Resolved Infrared and X-ray Absorption Spectroscopies

Yuushi Shimoda[1], Kiyoshi Miyata[1], Masataka Funaki[2], Tatsuki Morimoto[3], Shunsuke Nozawa[4,*], Shin-ichi Adachi[4], Osamu Ishitani[2], and Ken Onda[1,*]

[1]Department of Chemistry, Faculty of Science, Kyushu University, Motooka, Nishi-ku, Fukuoka 819-0395, Japan

[2]Department of Chemistry, School of Science, Tokyo Institute of Technology, O-okayama, Meguro-ku, Tokyo 152-8551, Japan

[3]Department of Applied Chemistry, School of Engineering, Tokyo University of Technology, Katakuramachi, Hachioji City, Tokyo 192-0982, Japan.

[4]Photon Factory, Institute of Materials Structure Sciences, High Energy Accelerator Research Organization (KEK), Oho, Tsukuba, Ibaraki 305-0801 Japan

*Corresponding authors: konda@chem.kyushu-univ.jp, noz@post.kek.jp

Abstract:

We have explored the structural factors on the photophysical properties in two rhenium(I) diimine complexes in acetonitrile solution, *cis*,*trans*-$[Re(dmb)(CO)_2(PPh_2Et)_2]^+$ (Et(2,2)) and *cis*,*trans*-$[Re(dmb)(CO)_2(PPh_3)_2]^+$ ((3,3)) (dmb = 4,4'-dimethyl-2,2'-bipyridine, Ph = phenyl, Et = ethyl) using the combination method of time-resolved infrared spectroscopy, time-resolved extended X-ray absorption fine structure, and quantum chemical calculations. The difference between these complexes is the number of phenyl groups in the phosphine ligand, and this only indirectly affects the central Re(I). Despite this minor difference, the complexes exhibit large differences in emission wavelength and excited-state lifetime. Upon photoexcitation, the bond length of Re-P and angle of P-Re-P are significantly changed in both complexes, while the phenyl groups are largely rotated by ~20º only in (3,3). In contrast, there is little change in charge distribution on the phenyl groups when Re to dmb charge transfer occurs upon photoexcitation. We concluded that the instability from steric effects of phenyl groups and diimine leads to the smaller Stokes shift of the lowest excited triplet state (T_1) in (3,3). The large structural change between the ground and excited states causes the longer lifetime of T_1 in (3,3).

1. Introduction

Rhenium(I) diimine biscarbonyl complexes that bear two phosphine ligands with various numbers of allyl groups or alkyl groups are widely known as efficient redox photosensitizers in photocatalytic systems for CO_2 reduction [1-6]. These complexes are good building blocks for linear-shaped [7,8] or ring-shaped [9-12] Re(I) multinuclear complexes. Such complexes have been used in various applications as photofunctional materials such as light harvesting materials [8,13], efficient photosensitizers [9,12], and multielectron storage molecules [10]. A useful characteristic of these complexes for these applications is that their photophysical and photochemical properties are controllable by varying the number and type of functional groups of the two phosphine ligands [4,6].

In general, the redox potentials, absorption, and emission wavelengths in these complexes are linearly dependent on the sum of the Tolman's χ values, which are an index of the electron accepting ability of phosphine ligands [4,6]. There are deviations from these trends when the complexes bear different numbers of aryl groups [6]. In particular, the Stokes shifts, which are the difference between absorption and emission energies, significantly decrease and the excited state lifetimes significantly increase when the complexes bare three aryl groups. These characteristics in the complexes bare three aryl groups are favorable for redox photosensitizers. In a previous report [6], these deviations were attributed to π-π interaction between the aryl groups of the two phosphine ligands and a diimine ligand. The π-π interaction is a generic concept that includes various interactions from attractive to repulsive forces between aromatic rings [14-17]. In the current study we examined the electronic and structural properties of two prototypical complexes in the excited-state using time-resolved infrared vibrational spectroscopy (TR-IR), time-resolved extended X-ray absorption fine structure (TR-EXAFS), and quantum chemical calculations.

TR-IR is a powerful tool for studying metal complexes in the excited state [18]. In particular, the IR spectra of double bonds such as C=C and C=N stretching vibrational modes in the finger-print region are good probes for the electronic and structural character of aromatic groups in the excited state, for aromatic ligands in metal complexes [19-23], and organic compounds [24-27]. There are two major advantages to studying intramolecular interactions in molecules containing aromatic groups using TR-IR. One is that a geometry for the lowest excited triplet state (T_1) can be determined in combination with quantum chemical calculations [20-23]. This is because T_1 is the lowest triplet state so optimized geometries can be calculated without considering configuration interactions or having to use time-dependent density functional theory (TD-DFT). This was confirmed using prototypical $[Ru(bpy)_3]^{2+}$ and its ligand- and isotope-substituted complexes [20,23]. The other major advantage is that correlations between photophysical properties and structural dynamics can be derived from temporal evolutions of TR-IR spectra [19,

21, 24-27]. The wavenumber and intensity of vibrational modes including double-bond vibrations are sensitive to the bond order and structure. Variations in bond order and structure can therefore be traced after photoexcitation in real-time. Using this method, we revealed that inter- and intra-molecular interactions between aromatic groups play an important role for photophysical properties such as photoinduced phase transition materials [19, 24, 25], photoactive liquid crystals [26], and thermally-activated delayed fluorescence materials [27].

The lowest photoexcited state in Re(I) diimine complexes is the metal-to-ligand charge transfer (MLCT) state. Thus, the positions of atoms adjacent to the central Re(I) atom are key for understanding the structural dynamics upon photoexcitation. EXAFS is one of the best methods to determine the positions of atoms adjacent to metal atoms [28,29]. It has recently become possible to measure TR-EXAFS of a metal complex in solution in sub-nanosecond time resolution with high sensitivity comparable to that of TR-IR [30-36]. TR-EXAFS provides complementary information to TR-IR on the structure of metal complexes. This is because TR-IR spectra above 1000 cm^{-1} are sensitive to vibrations within ligands but not to vibrations between a central metal atom and ligands.

In this study, we focus on two Re(I) diimine biscarbonyl complexes that have very different photophysical properties despite their similar molecular structures. One is *cis*, *trans*-$[Re(dmb)(CO)_2(PPh_2Et)_2]^+[PF_6]^-$ (dmb = 4,4'-dimethyl-2,2'-bipyridine, Ph = phenyl, Et = ethyl) (Et(2,2), Figure 1a) and the other is *cis*, *trans*-$[Re(dmb)(CO)_2(PPh_3)_2]^+[PF_6]^-$ ((3,3), Figure 1b). According to the previous report [6], the absorption wavelengths of Et(2,2) and (3,3) to ^{1}MLCT (metal-to-ligand charge-transfer state) are almost the same at 403 and 402 nm, respectively. However, their emission wavelengths from ^{3}MLCT are very different at 622 and 600 nm, respectively. This indicates that the Stokes shift of (3,3), 8200 cm^{-1}, is significantly smaller than that of Et(2,2), 8700 cm^{-1}. The lifetime of ^{3}MLCT of (3,3) is 1280 ns, which is more than twice as long as that of Et(2,2) at 646 and 203 ns (dual emission). The higher energy (because of the small Stokes shift) and longer lifetime of ^{3}MLCT of (3,3) should make (3,3) a better redox photosensitizer than Et(2,2).

To explore the difference in photophysical properties between Et(2,2) and (3,3) in terms of excited-state character, we measured TR-IR spectra in the wavenumber range from 1000 to 2200 cm^{-1} and carried out spectral simulations using DFT calculations. To confirm the assignments of vibrational modes, we carried out measurements on deuterated (3,3) in which all hydrogen atoms of phenyl groups were replaced by deuterium ((3D, 3D), Figure 1c). We measured TR-EXAFS under almost the same conditions as the TR-IR measurements, and analyzed the positions of atoms adjacent to Re(I). We discuss in detail the electronic and structural character based on geometries confirmed by TR-IR and TR-EXAFS. We found little difference in the electronic properties but a large difference in the excited-state structures between Et(2,2) and (3,3), which

should cause the difference in photophysical properties.

2. Experimental

2.1. Materials. All complexes were synthesized according to a previous report [6].

2.2. Instrumentation. Detailed procedures of steady-state IR and TR-IR measurements are reported elsewhere [18,23]. The steady-state IR spectra were measured by a Fourier-transform infrared (FT-IR) spectrometer (Shimadzu Prestage-21). KBr pellets for FT-IR measurements were prepared from 1.0 mg of sample and 150 mg of KBr powder. TR-IR spectra were acquired by a purpose-built system based on the pump-probe method, using a femtosecond Ti:sapphire chirped pulse amplifier (Spectra Physics Spitfire Ace, pulse duration = 120 fs, wavelength = 800 nm, repetition rate = 1 kHz). The pump pulse (wavelength = 400 nm, fluence at sample position = 7 mJ/cm^2) was generated using the second harmonic generation of part of the amplifier output. The tunable probe pulse (wavenumber range = 1000–4000 cm^{-1}, bandwidth = 150 cm^{-1}) was obtained by an optical parametric amplifier equipped with a crystal for difference frequency generation (Lighconversion, TOPAS-Prime). The pump and probe pulses were irradiated on an infrared flow cell with BaF_2 windows (optical path length = 0.1 or 0.5 mm). The polarizations of the pump and probe pulses on the flow cell were set to the magic angle using half wave plates for visible and mid-infrared wavelengths to avoid the effect of rotational relaxation. The spectrum of each probe pulse after passing through the flow cell was recorded by a mercury-cadmium-tellurium (MCT) infrared linear array system (Infrared Systems Development FpAS-64166-D). TR-IR spectra were obtained by averaging the difference between those with and without the pump pulse using an optical chopper synchronized with the pump pulse. The wavenumber resolution was 1–3 cm^{-1}, which depends on wavenumber because of the linearity of polychromator. The accuracy of the wavenumber was calibrated by comparing to the spectrum of a polystyrene film to within 2 cm^{-1}. Typical samples for TR-IR measurements were 3 mM acetonitrile solutions, which were bubbled with nitrogen gas before and during each measurement. All measurements were carried out at room temperature.

TR-EXAFS experiments with the pump-probe method were conducted at the AR-NW14A beamline in the Photon Factory Advanced Ring (PF-AR) [37]. The pump pulse (wavelength = 343 nm, fluence at sample position = 6 mJ/cm^2) was generated by the third harmonic generation of a femtosecond Yb fiber laser (Amplitude Tangerine). TR-EXAFS spectra were collected in fluorescence mode using a plastic scintillation detector. To measure the spectral change by the laser excitation precisely, the fluorescence X-ray signals before and after laser excitation were measured by gated integrators synchronized with the laser pulse (397 kHz). The sample (5 mM acetonitrile solution) was circulated using a diaphragm pump to reduce radiation damage by the

laser and X-ray, and was shaped to a stable 450-μm-thick jet using a stainless steel nozzle.

2.3. Quantum chemical calculations. All quantum chemical calculations were performed using the Gaussian16 software package [38]. The geometries of the ground state (S_0) and T_1 were optimized by DFT calculation using the mPW1PW91 functional and the LanL2DZ basis set. Solvent effects of acetonitrile were considered using the conductor-like polarizable continuum model. The IR vibrational spectra of S_0 and T_1 were simulated on the basis of the optimized geometries, and difference spectra corresponding to experimental TR-IR spectra were obtained by subtracting the S_0 spectra from the T_1 spectra. To fit the calculated spectra to the experimental spectra, we considered the bandwidth = 10 cm^{-1} and a scaling factor = 0.97 for vibrational modes at wavenumbers less than 1650 cm^{-1} [20] and a scaling factor = 1.02 for CO stretching vibrational modes ranging from 1750 to 2050 cm^{-1} [39]. To discuss changes in charge distribution upon electronic transition by photoexcitation, we performed TD-DFT calculations and obtained natural transition orbitals (NTOs) [40].

3. Results and Discussion

3.1. Experimental and calculated spectra and vibrational mode assignments

Figures 2a and 2c show the FT-IR spectra and Figures 2b and 2d show the calculated spectra of Et(2,2) and (3,3), respectively. The intensities less than 1650 cm^{-1} are shown enlarged for clarity. The FT-IR and calculated spectra are in good agreement with each other for both complexes, so we assigned the observed vibrational bands to the normal vibrational modes obtained by the calculations. The colors indicate the ligand at which the vibrations of each vibrational mode are mainly localized, judging from the view of the vibrational mode obtained by the calculations (Figure S1–S4). Peaks in blue, green, red, and gray are mainly localized at CO, dmb, Ph, and Et, respectively. Roughly speaking, the bands at 1850–1950 cm^{-1} are assigned to CO stretching vibrational modes while those at <1650 cm^{-1} are assigned to dmb and Ph.

Figures 3a and 3c show the TR-IR spectra at 100 ps of Et(2,2) and (3,3), respectively, and Figures 3b and 3d show their corresponding calculated spectra. These spectra show the difference in absorbance (Δabs) spectra between the ground and excited states. Upward and downward bands are assigned to vibrational transitions in the excited (transient absorption band) and ground states (bleach band), respectively. The TR-IR and calculated spectra are also in good agreement with each other for both complexes, so it is reasonable to discuss the character of T_1 based on these calculations. In the same manner as above, we assigned the bands to normal vibrational modes and the colors indicate the same groups as those for the FT-IR results. There are two distinctive features in these spectra. One is that the wavenumbers of bands assigned to CO (indicated by blue) are increased by 40–70 cm^{-1} compared with the corresponding bleach bands. These blue

shifts are well known and indicate that the charge at Re is reduced by the charge transfer from Re to dmb upon photoexcitation, and the C-O bands are strengthened by a decrease in π back-donation from Re [41-44]. The other distinctive feature is that almost all bands at wavenumber <1650 cm^{-1} (indicated by green) except that at 1100 cm^{-1} (indicated by red) are assigned to vibrational modes of dmb, which is largely different from the ground state spectra. This feature strongly indicates that charge variations by the charge transfer occur mainly on dmb. This speculation is supported by the NTO analysis from DFT calculations, which is described later.

To confirm our vibrational mode assignments, we measured the TR-IR spectra and carried out spectral simulations of (3D,3D). The measured and calculated results are shown in Figure 4a and 4b, respectively. The normal mode vibrations assigned to Ph are strongly localized in Ph (Figure S4), so the deuteration of Ph only affects the vibrations in Ph. The overall features of both the measured and calculated spectra are almost the same as those of (3,3) (Figure S5), indicating that there are few bands assigned to vibrational modes localized in Ph. However, carefully comparing the spectra of (3,3) in Figure 3c and (3D,3D) in Figure 4a reveals that the shapes of the bands assigned to Ph (indicated in red at approximately 1100 cm^{-1} in Figure 3c) are different. To show this difference more clearly, the TR-IR spectra of (3,3) and (3D,3D) are compared in the range from 1085 to 1130 cm^{-1} in Figure 4c. Although there is little difference in spectral shape at 1100–1120 cm^{-1}, the transient absorption and bleach bands at 1085–1100 cm^{-1} are only observed in (3,3). This indicates that these bands are assigned to vibrations localized in Ph. This result strongly suggests that the bands at 1085–1100 cm^{-1} are a good probe for changes in the character of Ph upon photoexcitation.

3.2. Temporal evolutions of TR-IR spectra

Temporal evolutions of TR-IR are useful for understanding the electronic and structural character of ligands in photoexcited states. We measured temporal evolutions of the TR-IR spectra of Et(2,2) and (3,3) in three wavenumber regions where typical bands assigned to each ligand are located: 1825–2050 cm^{-1} for CO (Figure 5), 1180–1260 cm^{-1} for dmb (Figure 6), and 1075–1120 cm^{-1} for Ph (Figure 7). In each figure, (a) and (b) show data of Et(2, 2) and (3, 3), respectively. The effects of rotational relaxation on the spectra were canceled by the magic angle configuration.

In Figures 5a and 5b, the two bleach bands show little spectral change up to 100 ps, whereas the transient absorption bands show slight blueshift and bandwidth narrowing within 10 ps. These trends in spectral evolution are almost the same as those in Figures 6a and 6b. On the basis of the spectral simulations obtained by the quantum chemical calculations, the bands in Figures 5 and 6 are assigned to the vibrations purely localized on CO and dmb, respectively. Except for the slight blueshift and narrowing, which result from vibrational relaxation in the excited states [41], the large wavenumber shifts of these transient absorption bands from those in the ground state occur

less than 1 ps after photoexcitation. This indicates the charge transfer from Re to dmb occurs immediately after photoexcitation. No change in bleach bands up to 100 ps indicates that there is no relaxation process to the ground state up to100 ps.

In contrast, the temporal evolutions of bands in Figure 7 are very different from those in Figures 5 and 6. On the basis of the calculations, vibrational bands in this region largely contain vibrations of Ph. Ph therefore has different dynamics from the other ligands in the early process after photoexcitation. The band at 1100 cm^{-1} in Figure 7a, which consists of normal vibrational modes strongly localized on Ph, increases gradually from 1 to 100 ps though it starts at a negative value because of overlapping with a bleach band. The band at 1100 cm^{-1}, which consists of vibrational modes of both dmb and Ph, also increases gradually from 1 to 30 ps after the sudden increase at 1 ps. In Figure 7b, the temporal behaviors of the bands are almost the same as those in Figure 7a, except that the overlapping between the transient absorption band and bleach band is much larger in the range from 1087 to 1097 cm^{-1}.

To show the different dynamics of each ligand clearly, we plot the intensities of typical bands at 1971–1976 cm^{-1} for CO (blue squares), at 1212–1214 and 1214–1217 cm^{-1} for dmb (green squares), and at 1098 and 1093 cm^{-1} for Ph (red squares), as a function of delay time in Figures 8a and 8b for Et(2,2) and (3,3), respectively. The intensities of the bands for CO and dmb were estimated by fitting to Gaussian functions to cancel the effects of the blueshift and narrowing. For the intensities of the bands for Ph, the ΔAbs at 1198 cm^{-1} for Et(2,2) and the ΔAbs at 1193 cm^{-1} for (3,3) were simply plotted because it is difficult to extract one band from the experimental spectra consisting of several transient absorption and bleach bands. For all three plots, the intensities change greatly less than 1 ps after photoexcitation followed by a gradual increase over 10 ps for CO and dmb and over 50 ps for Ph. The time constants of these gradual increases were estimated using a single exponential function. The estimated time constants for Et(2,2) in Figure 8a are 1.2 ± 0.1 ps for CO, 2.0 ± 0.1 ps for dmb, and 30.8 ± 1.4 ps for Ph, and those for (3,3) in Figure 8b are 1.2 ± 0.1 ps for CO, 3.7 ± 0.3 ps for dmb, and 25.2 ± 0.7 ps for Ph. These results strongly indicate that phenyl groups in the phosphine ligands in both complexes do not undergo structural changes immediately after charge transfer from Re to dmb by photoexcitation. Rather, it takes more than 20 ps for their structural changes to occur after charge transfer.

3.3. TR-EXAFS determination of atomic displacements adjacent to Re atom

To determine directly the positions of atoms adjacent to the central Re(I) atom, we measured TR-EXAFS of (3,3) at the Re-LIII absorption edge. Details of the analysis can be found in the supporting information. For S_0 and T_1, EXAFS spectra weighted by k^3 (k: wavenumber) and their Fourier-transformed (FT) spectra are shown in Figure 9a–d. The EXAFS spectrum of T_1 was measured at 100 ps after photoexcitation in which the movement of the ligands subsided. In the

FT spectra of both S_0 (Figure 9b) and T_1 (Figure 9d), a dominant contribution at ~1.0–2.3 Å is attributed to the first nearest neighbor (NN) of the Re-C in CO, the Re-N in dmb, and the Re-P in PPh_3. The feature appearing at ~2.3–3.2 Å results from contributions from the second NN of the Re-C in dmb and the Re-O in CO, and the multiple scatterings in dmb and CO. To investigate the local molecular structures around the Re atom in more detail, curve-fitting analysis was performed. The R range employed in the curve-fitting analysis was $\Delta R \approx 1$–3.2 Å. Fitting results are shown in Figure 9 as dotted lines. The bond lengths of the first NN obtained from the EXAFS analysis are listed in Table 1 together with those obtained by the DFT calculations from the TR-IR analysis. These values are in good agreement with each other. Also, the values for S_0 are very close to those in a single crystal obtained by X-ray diffraction analysis [6]. These results strongly indicate that the optimized geometries by DFT calculations are highly reliable.

The differences in bond length between S_0 and T_1 are qualitatively explained by the fact that T_1 is the MLCT state. Charge transfer from Re to dmb decreases the charge on Re and increases that on dmb. The bonds between Re and CO and between Re and dmb have d-π interaction as well as coordination bond whereas that between Re and a phosphine ligand has only coordination bond. A decrease in charge on Re decreases the d-π interaction in Re-C bond between Re and CO (a decrease in π-back donation) and increases the bond length between Re and C. The bond between Re and dmb undergoes an increase in charge on dmb in addition to a decrease in charge on Re; thus, the d-π interaction somewhat increases and the bond lengths between Re and N increase. In contrast, the bond length between Re and P increase by a decrease in charge on Re because the bond between Re and a phosphine ligand has no d-π interaction.

Table 1. Bond lengths and mean-square displacements σ^2 in S_0 and T_1 obtained by the EXAFS fitting in (3,3), and calculated values obtained by the DFT calculations.

bond	S_0			T_1		
	length (Å)		σ^2 (Å^2)	length (Å)		σ^2 (Å^2)
	calc.	EXAFS	EXAFS	calc.	EXAFS	EXAFS
Re−C1	1.89	1.86(2)	0.008(2)	1.96	1.95(2)	0.016(13)
Re−C2	1.89	1.86(2)	0.008(2)	1.90	1.89(2)	0.016(13)
Re−P1	2.51	2.41(2)	0.004(2)	2.56	2.54(2)	0.005(3)
Re−P2	2.51	2.41(2)	0.004(2)	2.56	2.54(2)	0.005(3)
Re−N1	2.16	2.13(5)	0.004(4)	2.14	2.11(2)	0.001(1)
Re−N2	2.15	2.13(5)	0.004(4)	2.05	2.03(2)	0.001(1)

3.4. NTOs and geometries in S_0 and T_1

The calculated difference spectra between T_1 and S_0 are in good agreement with the TR-IR spectra and also the optimized geometries are confirmed by the TR-EXAFS spectra. The optimized geometries in S_0 and T_1 are therefore sufficiently reliable for further discussion on molecular orbitals and molecular structures. Figure 10 shows NTOs in S_0 and T_1 for Et(2, 2). NTOs were calculated by TD-DFT based on the optimized geometries, and they express the variation in charge distribution upon transition [40]. For both S_0 and T_1 geometries, the highest occupied NTO (HONTO) is distributed mainly at Re and slightly at CO and dmb, whereas the lowest unoccupied NTO (LUNTO) is distributed mainly at dmb and slightly at CO but little at Re. This variation in orbital distribution indicates that charge at Re transfers to dmb, which agrees well with T_1 being assigned to the ^{3}MLCT state. In contrast to CO and dmb, NTOs are little distributed at Ph and there is almost no change in orbital distribution between the HONTO and LUNTO, indicating that phenyl groups do not undergo changes in charge distribution. These results explain why the structural change of phenyl groups occurs more slowly than charge transfer from Re to dmb after photoexcitation (described above). The phenyl groups are electronically isolated through the C-P-Re bond, so they are relocated by weak interactions with dmb and/or CO, which can be regarded as π-π interactions. This process should take several tens picoseconds using the analogy for the reorientation of surrounding solvent molecules. This mechanism also applies in (3, 3) because the HONTO and LUNTO are almost the same as those of Et(2, 2), as shown in Figure 11.

We now compare the optimized geometries between S_0 and T_1. For Et(2, 2), there are two geometries that have slightly different energies: one geometry has both Et groups on the same side (*cis*-Et(2, 2) in Figure 12) and the other geometry has one Et on either side (*trans*-Et(2, 2) in Figure 13). In these figures, the lower and upper geometries are S_0 and T_1, respectively. These geometries correspond to two of the conformers in the previous report [6], and they can be verified by comparing their calculated spectra with TR-IR spectra. The calculated difference spectra of these two geometries are almost the same, as shown in Figure S6. Thus, the predominant geometry in solution cannot readily be determined from the TR-IR spectra. The energy difference between these geometries is very small: 0.0069 eV in S_0 and 0.0207 eV in T_1, but the potential barrier between the two geometries should be much larger considering the reaction path. According to the previous report [6], the barrier heights are around 10 kJ/mol, which is much higher than the energy at room temperature (~2.5 kJ/mol). Thus, these two geometries are not likely to exchange at room temperature.

Figure 14 shows the optimized geometries in S_0 (lower) and T_1 (upper) for (3, 3). Tables S1 and S2 summarize structural parameters obtained from the calculations for Et(2, 2) and (3, 3), respectively. When the geometrical changes from S_0 to T_1 are considered, the common features in structural change between Et(2, 2) and (3, 3) are the elongation of Re-P bonds (0.05 Å in

Et(2, 2) and 0.05 Å in (3, 3)) and the reduction of P-Re-P angle (–4.6º in Et(2, 2) and –8.1º in (3, 3)). These structural changes should occur immediately after photoexcitation because P is coordinated directly to Re and Re is oxidized by the charge transfer from Re to dmb upon photoexcitation. Similar structural changes are reportedly observed in the dimer consisting of the same Re complex units [21]. The structures of CO and dmb are little changed by the charge transfer because the double or triple bonds in these ligands are stronger than P-Re. The electronic states of these ligands are largely changed by charge transfer because large spectral changes are observed immediately after photoexcitation.

In addition to these common features in structural change between Et(2, 2) and (3, 3), the rotations of phenyl groups on the C-P axis are different between Et(2, 2) and (3, 3). As shown in Tables S1 and S2, the phenyl groups are rotated by 1º or 2º in Et(2,2) and by 16–27º in (3, 3), with respect to the ground state angles. The intensities of vibrational bands assigned to Ph increase more slowly than the other bands, so these rotations occur much later after the charge transfer upon photoexcitation. There is little change in charge distribution in the phenyl groups upon photoexcitation, indicating that there is little change in electronic interaction of the phenyl groups with other ligands. Thus, these structural changes occur not by direct change in electronic states by the charge transfer but by indirect change induced by the elongation of Re-P bonds.

3.5. Correlation between photophysical properties and excited state structures

According to the report [6], there are two characteristics of photophysical properties in (3,3) compared with (2,2) and other complexes:

(1) The Stokes shift of (3,3) is much smaller than that of Et(2,2),

(2) The lifetime of T_1 in (3,3) is much longer than that in Et(2,2).

Our experiments and calculations revealed the following characteristics in terms of electronic state and molecular geometry:

(i) Charge transfer occurs only in the plane consisting of Re, CO, and dmb, and has no direct effect on Ph,

(ii) Only Ph undergoes structural change slowly (25–30 ps) after photoexcitation.

Therefore, phenyl groups in the phosphine ligands show different behavior upon photoexcitation, and this behavior is expected to originate from indirect interactions.

The next question is how these experimental observations explain the difference in photophysical properties. Regarding characteristic (1), the quantum chemical calculations of T_1, which are well supported by TR-IR and TR-EXAFS, effectively reproduce this characteristic as shown in the energy diagram in Figure 15. This means that the calculations include the origin of this characteristic. Close inspection of the distances among the functional groups in the filling models obtained from the calculations (Figure 16) shows that the phenyl group above dmb in

Et(2,2) is more parallel to the dmb plane than that in (3,3). This is probably because the phenyl groups in (3,3) are so crowded that they are rotated to avoid steric repulsions. This rotation reduces the attractive π-π interaction between the phenyl group and dmb in (3,3) and increases the repulsive force among the phenyl groups and dmb. This is why T_1 in (3,3) is higher in energy than that in Et(2,2). Figure 17 shows schematic potentials depicting this situation. The crowded phenyl groups in (3,3) create the shallow potential because of steric repulsion, which makes the phenyl groups readily rotate. The deeper potentials because of the non-crowded phenyl groups in Et(2,2) restrict the rotation of phenyl groups. This difference in potential also explains why the Stokes shift of (3,3) is smaller than that of Et(2,2).

Regarding characteristic (2) requires considering how the lifetime of T_1 is determined in these complexes. In general, a lowest triplet excited state has a very long lifetime of more than a millisecond because of spin forbidden transition. The main relaxation paths to the ground state in these types of metal complexes are direct relaxation from T_1 to S_0 potentials unless another excited state exists that is close in energy to T_1. This type of non-radiative relaxation was studied semi-quantitatively by Engleman and Jortner [45]. They derived a simple law named the "energy gap law": The relaxation rate is determined by the overlap between wavefunctions of the excited and ground state potentials at the same energy level (Franck-Condon factor). Roughly speaking, a larger energy gap between two potentials gives a smaller Franck-Condon factor and a smaller relaxation rate if the equilibrium positions of the two potentials are close (Figure 18a). A larger difference in equilibrium position gives a larger Franck-Condon factor and a larger relaxation rate if the energy gap is the same (Figure 18b). However, these simple predictions are not reasonable for a molecule in which there is a large difference in molecular structure between the ground and excited states such as in our complexes. Particularly the assumption described in Ref. [45]: "We assume that the normal modes and their frequencies are the same in the two electronic states except for displacements in the origins of the normal coordinates.", is not valid for a complex that undergoes a large structural change upon photoexcitation such as (3,3). This deviation from the simple model is known as the Duschinsky effect [46, 47]. Nevertheless, quantitative estimation of this effect is difficult for a complicated system such as in our complexes, so here we consider it qualitatively. If the normal coordinate of T_1 is largely different from that of S_0, the Franck-Condon factor becomes small, as shown schematically in Figure 18c. The energy gap law considering this effect can explain characteristic (2). While the structural change between T_1 and S_0 in (3,3) is large, that in (2,2) is small. Thus, the total Franck-Condon factor in (3,3) is smaller than that in (2,2), so the lifetime of T_1 in (3,3) becomes longer than that in (2,2). This situation is the same as that for the dimer consisting of the same Re complex units we reported previously [21].

4. Summary

We investigated the photophysical properties of two phenylphosphine Re(I) diimine biscarbonyl complexes, one bearing two phenyl groups and one ethyl group, Et(2,2), and the other baring three phenyl groups, (3,3), in one phenylphosphine ligand. The different photophysical properties of these two complexes cannot be explained solely by the electron accepting ability of the phosphine ligands. Thus, we compared their excited state dynamics using the combination method of TR-IR, TR-EXAFS, and DFT calculations. Their TR-IR spectra are effectively reproduced by the DFT calculations, assuming that the ground and excited states are the lowest singlet (S_0) and lowest triplet (T_1) states, respectively. Normal vibrational mode analyses were carried out based on the calculations and comparison to spectra of a deuterated complex. The temporal evolutions of TR-IR spectra indicate that the phenyl groups undergo structural change more slowly (by ~20–30 ps) than the other ligands (<1 ps). The positions of atoms adjacent to Re were determined by TR-EXAFS, which are consistent with the geometries obtained by the DFT calculations.

The natural transition orbital analysis indicates that photoexcitation induces charge transfer from Re to the diimine ligands but no change in charge at the phenyl groups. From the optimized geometries of S_0 and T_1, the bond length of Re-P and the angle of P-Re-P are changed to a similar degree in both complexes, while the phenyl groups are largely rotated by 16–21^o only in (3,3). These results indicate that that displacements of phenyl groups occur indirectly via steric interaction among the aromatic groups, phenyl groups, and diimine. We therefore concluded that the triplet excited state in (3,3) being located higher in energy than that in Et(2,2) originates from the steric instability; this is because of the congestion of the phenyl groups in (3,3). The longer lifetime of (3,3) is attributed to the reduced non-radiative relaxation from the smaller overlap of wavefunctions between S_0 and T_1 because of the large displacements of phenyl groups, which is a special case of the energy gap law. This correlation between photophysical properties and structural dynamics indicates that photophysical properties in metal complexes can be controlled by carefully placing ligands while considering their steric interactions. In addition, our study shows that the combination method of TR-IR and TR-EXAFS makes it possible for us to explore photophysical and photochemical properties in metal complexes in terms of excited-state structure.

Acknowledgements

This work was supported by JSPS KAKENHI Grant Numbers JP17H06375, JP17H06438, JP17H06372, JP17H06141, JP18H05170, JP19H05782, JP20H05106 and JST CREST Grant Number JPMJCR13L1. The computations were performed at the Research Institute for Information Technology (Kyushu University, Japan).

Supporting Information.

Selected normal vibrational modes of Et(2,2) and (3,3), comparison of TR-IR spectra of (3,3) and (3D,3D), FT-IR and TR-IR spectra of *cis*- and *trans*-Et(2,2), selected bond lengths and dihedral angles in the optimized geometries of Et(2,2) and (3,3), details of EXAFS analysis.

References

(1) Yamazaki, Y.; Takeda, H.; Ishitani, O. Photocatalytic reduction of CO_2 using metal complexes, *J. Photochem. Photobio. C: Photochem. Rev.* **2015**, *25*, 106-137.

(2) Ishitani, O.; George, M. W.; Ibusuki, T.; Johnson, F. P. A.; Koike, K.; Nozaki, K.; Pac, C.; Turner, J. J.; Westwell, J. R. Photophysical Behavior of New CO_2 Reduction Catalyst, $Re(CO)_2(bpy)\{P(OEt)_3\}_2^+$, Inorg. Chem. **1994**, *33*, 4712-4717.

(3) Koike, K.; Tanabe, J.; Toyama, S.; Tsubaki, H.; Sakamoto, K.; Westwell, J. R.; Johnson, F. P. A.; Hori, H.; Saitoh, H.; Ishitani, O. New Synthesis Routes to Biscarbonylbipyridinerhenium(I) Complexes *cis*, *trans*-$[Re(X_2\text{-bpy})(CO)_2(PR_3)(Y)]^{n+}$ (X_2bpy = 4,4'-X_2-2,2'-bipyridine) via photochemical Ligand Substitution Reactions, and Their Photophysical and Electrochemical Properties, *Inorg. Chem.* **2000**, *39*, 2777-2783.

(4) Tsubaki, H.; Sekine. A.; Ohashi, Y.; Koike, K.; Takeda, H.; Ishitani, O. *J. Am. Chem. Soc.* **2005**, *127*, 15544-15555.

(5) Takeda, H.; Koike, K.; Inoue, H.; Ishitani, O. Development of an Efficient Photocatalytic System for CO_2 Reduction Using Rhenium(I) Complexes Based on Mechanistic Studies. *J. Am. Chem. Soc.* **2008,** *130*, 2023-2031.

(6) Morimoto, T.; Ito, M.; Koike, K.; Kojima, T.; Ozeki, T.; Ishitani, O. Dual Emission from Rhenium(I) Compelxes Induced by and Interligand Aromatic Interaction, *Chem. Eur. J.* **2012**, *18*, 3292-3304.

(7) Yamamoto, Y.; Sawa, S.; Funada, Y.; Morimoto, T.; Falkenström, M.; Miyasaka, H.; Shishido, S.; Ozeki, T.; Koike, K.; Ishitani, O. Systematic Synthesis, Isolation, and Photophysical Properties of Linear-Shaped Re(I) Oligomers and Polymers with 2−20 Units. *J. Am. Chem. Soc.* **2008,** *130*, 14659-14674.

(8) Yamamoto, Y.; Tamaki, Y.; Yui, T.; Koike, K.; Ishitani, O. New Light-Harvesting Molecular Systems Constructed with a Ru(II) Complex and a Linear-Shaped Re(I) Oligomer. *J. Am. Chem. Soc.* **2010,** *132*, 11743-11752.

(9) Morimoto, T.; Nishiura, C.; Tanaka, M.; Rohacova, J.; Nakagawa, Y.; Funada, Y.; Koike, K.; Yamamoto, Y.; Shishido, S.; Kojima, T.; Saeki, T.; Ozeki, T.; Ishitani, O. Ring-Shaped Re(I) Multinuclear Complexes with Unique Photofunctional Properties. *J. Am. Chem. Soc.* **2013,** *135*,

13266-13269.
(10) Asatani, T.; Nakagawa, Y.; Funada, Y.; Swa, S.; Takeda, H.; Morimoto, T.; Koike, K.; Ishitani, O. Ring-Shaped Rhenium(I) Multinuclear Complexes: Improved Synthesis and Photoinduced Multielectron Accumulation, *Inorg. Chem.* **2014**, *53*, 7170-7180.
(11) Rohacova, J.; Sekine, A.; Kawano, T.; Tamri, S.; Ishitani, O. Trinuclear nad Tetranuclear Re(I) Rings Connencted with Phenylene Vinylene, and Ethynylene Chains: Synthesis, Photophysics, and Redox Properties, *Inorg. Chem.* **2015**, *54*, 8769-8777.
(12) Rohacova, J.; Ishitani, O. Rhenium(I) trinuclear rings as highly efficient redox photosensitizers for photocatalytic CO_2 reduction, *Chem. Sci.* **2016**, *7*, 6728-6739
(13) Yamamoto, Y.; Takeda, H.; Yui, T.; Ueda, Y.; Koike, K.; Inagaki, S.; Ishitani, O., Efficient light harvesting via sequential two-step energy accumulation using a Ru-Re5 multinuclear complex incorporated into periodic mesoporous organosilica. *Chemical Science* **2014**, 5, 639-648.
(14) Martinez, C. R.; Iverson, B. L. Rethinking the term ‘‘pi-stacking’’, *Chem. Sci.* **2012**, *3*, 2191-2201.
(15) Hunter, C. A.; J. K. M. Sanders, The Nature of π-π Interactions, *J. Am. Chem. Soc.* **1990**, *112*, 5525-5534.
(16) Hunter, C. A. Lawson, K. R.; Perkins, J.; Urch, C. J. Aromatic interactions, *J. Chem. Soc., Perkin Trans*, **2001**, *2*, 651-669.
(17) Sinnokrot, M. O.; Valeev, E. F.; Sherrill, C. D. Estimates of the Ab Initio Limit for π-π Interactions: The Benzene Dimer, *J. Am. Chem. Soc.* **2002**, *124*, 10887-10893.
(18) Butler, J. M.; George M. W.; Schoonover, J. R.; Dattelbaum, D. M.; Meyer, T. J. *Coord. Chem. Rev.* **2007**, *251*, 492-514.
(19) Fukazawa, N.; Tanaka, T.; Ishikawa, T.; Okimoto, Y.; Koshihara, S.; Yamamoto, T.; Tamura, M.; Kato, R.; Onda, K. Time-Resolved Infrared Vibrational Spectroscopy of the Photoinduced Phase Transition of $Pd(dmit)_2$ Salts Having Different Orders of Phase Transition, *J. Phys. Chem. C*, **2013**, *117*, 13187-13196.
(20) Mukuta, T.; Fukazawa, N.; Murata, K.; Inagaki, A.; Akita, M.; Tanaka, S.; Koshihara, S.; Onda, K. Infrared Vibrational Spectroscopy of $[Ru(bpy)_2(bpm)]^{2+}$ and $[Ru(bpy)_3]^{2+}$ in the Excited Triplet State. *Inorg. Chem.* **2014,** *53*, 2481-2490.
(21) Tanaka, S.; Takahashi, K.; Hirahara, M.; Yagi, M.; Onda, K. Characterization of the excited states of *distal*- and *proximal*-$[Ru(tpy)(pynp)OH_2]^{2+}$ in aqueous solution using time-resolved infrared spectroscopy. *J. Photochem. Photobiol., A* **2015,** *313*, 87-98.
(22) Zimmer, M. ; Rupp, F.; Singer, P.; Walz, F.; Breher, F.; Klopper, W.; Diller, R.; Gerhards, M. Time-resolved IR spectroscopy of a trinuclear palladium complex in solution, *Phys. Chem. Chem. Phys.* **2015**, *17*, 14138-14144.

(23) Mukuta, T.; Tanaka, S.; Inagaki, A.; Koshihara, S.; Onda , K. Direct Observation of the Triplet Metal-Centered State in $[Ru(bpy)_3]^{2+}$ Using Time-Resolved Infrared Spectroscopy. *ChemistrySelect* **2016,** *1*, 2802-2807.

(24) Matsubara, Y.; Okimoto, Y.; Yoshida, T.; Ishikawa, T.; Koshihara, S.; Onda, K. Photoinduced Neutral-to-Ionic Phase Transition in Tetrathiafulvalene-*p*-Chloranil Studied by Time-resolved Vibrational Spectroscopy, *J. Phys. Soc. Jpn*, **2011**, *80*, 124711-1 - -5.

(25) Fukazawa, N.; Shimizu, M.; Ishikawa, T.; Okimoto, Y.; Koshihara, S.; Hiramatsu, T.; Nakano, Y.; Yamochi, H.; Saito, G.; Onda, K. Charge and structural dynamics in photoinduced phase transition of $(EDO\text{-}TTF)_2PF_6$ examined by picosecond time-resolved vibrational spectroscopy, *J. Phys. Chem. C*, **2012**, *116*, 5892-5899.

(26) Hada, M.; Saito, S.; Tanaka, S.; Sato, R.; Yoshimura, M.; Mouri, K.; Matsuo, K.; Yamaguchi, S.; Hara, M.; Hayashi, Y.; Shigeta, Y.; Onda, K.; Miller, R. J. D. Structural Monitoring of the Onset of Excited-State Aromaticity, *J. Am. Chem. Soc.* **2017**, *139*, 15792-15800.

(27) Saigo, M.; Miyata, K.; Tanaka, S.; Nakanotani, H.; Adachi, C.; Onda, K. Suppression of Structural Change upon S_1-T_1 Conversion Assists Thermally Activated Delayed Fluorescence Process in Carbazole-Benzonitrile Derivatives, *J. Phys. Chem. Lett.* **2019**, *10*, 2475-2480.

(28) Sayers, D. E.; Stern, E. A.; Lytle, F. W., New technique for investigating noncrystalline structures: Fourier analysis of the extended x-ray—absorption fine structure. *Physical review letters* **1971,** *27* (18), 1204.

(29) Lytle, F. W., The EXAFS family tree: a personal history of the development of extended X-ray absorption fine structure. *Journal of Synchrotron Radiation* **1999,** *6* (3), 123-134.

(30) Gawelda, W.; Pham, V.-T.; Benfatto, M.; Zaushitsyn, Y.; Kaiser, M.; Grolimund, D.; Johnson, S. L.; Abela, R.; Hauser, A.; Bressler, C., Structural determination of a short-lived excited iron (II) complex by picosecond x-ray absorption spectroscopy. *Physical review letters* **2007,** *98* (5), 057401.

(31) Bressler, C.; Chergui, M., Molecular structural dynamics probed by ultrafast X-ray absorption spectroscopy. *Annual review of physical chemistry* **2010,** *61*, 263-282.

(32) Nozawa, S.; Sato, T.; Chollet, M.; Ichiyanagi, K.; Tomita, A.; Fujii, H.; Adachi, S.; Koshihara, S., Direct probing of spin state dynamics coupled with electronic and structural modifications by picosecond time-resolved XAFS. *Journal of the American Chemical Society* **2010,** *132* (1), 61-63.

(33) Penfold, T. J.; Milne, C. J.; Chergui, M., Recent advances in ultrafast x-ray absorption spectroscopy of solutions. *Adv. Chem. Phys* **2013,** *153*, 1-41.

(34) El Nahhas, A.; Van Der Veen, R. M.; Penfold, T. J.; Pham, V. T.; Lima, F. A.; Abela, R.; Blanco-Rodriguez, A. M.; Zalis, S.; Vlcek, A.; Tavernelli, I., X-ray absorption spectroscopy of ground and excited rhenium–carbonyl–diimine complexes: Evidence for a two-center electron

transfer. *The Journal of Physical Chemistry A* **2013,** *117* (2), 361-369.
(35) Milne, C. J.; Penfold, T. J.; Chergui, M., Recent experimental and theoretical developments in time-resolved X-ray spectroscopies. *Coordination Chemistry Reviews* **2014,** *277*, 44-68.
(36) Chergui, M., Ultrafast photophysics of transition metal complexes. *Accounts of Chemical Research* **2015,** *48* (3), 801-808.
(37) Nozawa, S.; Adachi, S. i.; Takahashi, J. i.; Tazaki, R.; Guérin, L.; Daimon, M.; Tomita, A.; Sato, T.; Chollet, M.; Collet, E., Developing 100 ps-resolved X-ray structural analysis capabilities on beamline NW14A at the Photon Factory Advanced Ring. *Journal of synchrotron radiation* **2007,** *14* (4), 313-319.
(38) Gaussian 16, Revision A.03, M. J. Frisch, G. W. Trucks, H. B. Schlegel, G. E. Scuseria, M. A. Robb, J. R. Cheeseman, G. Scalmani, V. Barone, G. A. Petersson, H. Nakatsuji, X. Li, M. Caricato, A. V. Marenich, J. Bloino, B. G. Janesko, R. Gomperts, B. Mennucci, H. P. Hratchian, J. V. Ortiz, A. F. Izmaylov, J. L. Sonnenberg, D. Williams-Young, F. Ding, F. Lipparini, F. Egidi, J. Goings, B. Peng, A. Petrone, T. Henderson, D. Ranasinghe, V. G. Zakrzewski, J. Gao, N. Rega, G. Zheng, W. Liang, M. Hada, M. Ehara, K. Toyota, R. Fukuda, J. Hasegawa, M. Ishida, T. Nakajima, Y. Honda, O. Kitao, H. Nakai, T. Vreven, K. Throssell, J. A. Montgomery, Jr., J. E. Peralta, F. Ogliaro, M. J. Bearpark, J. J. Heyd, E. N. Brothers, K. N. Kudin, V. N. Staroverov, T. A. Keith, R. Kobayashi, J. Normand, K. Raghavachari, A. P. Rendell, J. C. Burant, S. S. Iyengar, J. Tomasi, M. Cossi, J. M. Millam, M. Klene, C. Adamo, R. Cammi, J. W. Ochterski, R. L. Martin, K. Morokuma, O. Farkas, J. B. Foresman, and D. J. Fox, Gaussian, Inc., Wallingford CT, 2016.
(39) Tanaka, S.; Matsubara, Y.; Asatani, T.; Morimoto, T.; Ishitani, O.; Onda, K. Structural deformation of a ring-shaped Re(I) diimine dinuclear complex in the excited state. *Chem. Phys. Lett.* **2016,** *662*, 120-126.
(40) Martin, R. L. Natural transition orbitals, *J. Chem. Phys.* **2003**, *118*, 4775-4777.
(41) Sato, S.; Matubara, Y.; Koike, K.; Falkenström, M.; Katayama, T.; Ishibashi, Y.; Miyasaka, H.; Taniguchi, S.; Chosrowjan, H.; Mataga, N.; Fukazawa, N.; Koshihara, S.; Onda, K.; Ishitani, O. Photochemistry of fac-[Re(bpy)$(CO)_3$Cl]. *Chem. - Eur. J.* **2012,** 18, 15722-15734.
(42) Liard, D. J.; Busby, M.; Matousek, P.; Towrie, M.; Vlček, A. Picosecond Relaxation of ^{3}MLCT Excited States of [Re(Etpy)$(CO)_3$(dmb)]$^+$ and [Re(Cl)$(CO)_3$(bpy)] as Revealed by Time-Resolved Resonance Raman, UV−vis, and IR Absorption Spectroscopy. *J. Phys. Chem. A* **2004,** 108, 2363-2369.
(43) Li, G.; Parimal, K.; Vyas, S.; Hadad, C. M.; Flood, A. H.; Glusac, K. D. Pinpointing the Extent of Electronic Delocalization in the Re(I)-to-Tetrazine Charge-Separated Excited State Using Time-Resolved Infrared Spectroscopy. *J. Am. Chem. Soc.* **2009,** 131, 11656-11657.
(44) Dattelbaum, D. M.; Omberg, K. M.; Schoonover, J. R.; Martin, R. L.; Meyer, T. J. Application

of Time-Resolved Infrared Spectroscopy to Electronic Structure in Metal-to-Ligand Charge-Transfer Excited States. *Inorg. Chem.* **2002,** 41, 6071-6079.
(45) Engleman, R.; Jortner, J. The energy gap law for radiationless transitions in large molecules, *Mol. Phys.* **1970**, *18*, 145-164.
(46) Small, G. J. Herzberg-Teller Vibronic Coupling and the Duschinsky Effect, *J. Chem. Phys.* **1971**, *54*, 3300-3306.
(47) Mebel, A. M.; Hayashi, M.; Liang, K. K.; Lin, S. H. Ab Initio Calculations of Vibronic Spectra and Dynamics for Small Polyatomic Molecules: Role of Duschinsky Effect, *J. Phys. Chem. A*, **1999**, *103*, 10674-10690.

Figure captions

Fig. 1. Molecular structures of (a) *cis*, *trans*-[Re(dmb)$(CO)_2(PPh_2Et)_2]^+$ (Et(2,2)), (b) *cis*, *trans*-[Re(dmb)$(CO)_2(PPh_3)_2]^+$ ((3,3)), and (c) deuterated (3,3) ((3D, 3D)).

Fig. 2. Steady-state observed and calculated spectra of Et(2,2) and (3,3): (a) FT-IR spectra and (b) calculated IR spectra of the S_0 state of Et(2,2), (c) FT-IR spectra and (d) calculated IR spectra of the S_0 state of (3,3). The colors indicate the ligand on which the vibrations are predominantly localized: blue = CO, green = dmb, and red = Ph.

Fig. 3. Time-resolved observed and calculated spectra of Et(2,2) and (3,3): (a) TR-IR spectra and (b) calculated difference IR spectra between the T_1 and S_0 states of Et(2,2), (c) TR-IR spectra and (d) calculated difference IR spectra of the T_1 and S_0 states of (3,3). The colors indicate the ligand on which the vibrations are predominantly localized: blue = CO, green = dmb, and red = Ph.

Fig. 4. (a) TR-IR spectra and (b) calculated difference IR spectra between the T_1 and S_0 states of (3D,3D). (c) Comparison of the TR-IR spectra of (3,3), black line, and (3D,3D), red line.

Fig. 5. Temporal evolutions of the TR-IR spectra of (a) Et(2,2) and (b) (3,3) in the CO stretching vibrational mode region.

Fig. 6. Temporal evolutions of the TR-IR spectra of (a) Et(2,2) and (b) (3,3) in the region in which dmb vibrational modes are located.

Fig. 7. Temporal evolutions of the TR-IR spectra of (a) Et(2,2) and (b) (3,3) in the region in which Ph and dmb vibrational modes are located.

Fig. 8. Temporal profiles of the intensity estimated by fitting using a Gaussian function for bands assigned to CO (blue) and dmb (green), and of the absorbance change (Δabs.) at the position mainly assigned to Ph (red) in (a) Et(2,2) and (b) (3,3). See the text for details of the estimations.

Fig. 9. EXAFS of the S_0 (a) and T_1 (c) states, and Fourier-transformed (FT) EXAFS of the S_0 (b) and T_1 (d) states of (3,3). The EXAFS of the T_1 state is derived by eq. (1) in the supporting information, with the EXAFS of the S_0 state shown in (a), 1.4% of the fraction for T_1 at τ = 100 ps, and the transient EXAFS difference at 100 ps. In (a) and (c), the windows are for the Fourier transformation, and EXAFS data and their fitting results are indicated by the blue lines and orange

dotted lines, respectively. In (b) and (d), the windows are for the EXAFS fitting analysis. The experimental data of the real and imaginary parts of FT EXAFS are indicated by the blue and light-blue lines, respectively. The fitting results for the real and imaginary parts of FT EXAFS are indicated by the blue and light-blue dotted lines, respectively.

Fig. 10. Natural transition orbitals for the S_0 and T_1 states of Et(2,2).

Fig. 11. Natural transition orbitals for the S_0 and T_1 states of (3,3).

Fig. 12. Optimized geometries of the S_0 and T_1 states of *cis*-Et(2,2).

Fig. 13. Optimized geometries of the S_0 and T_1 states of *trans*-Et(2,2).

Fig. 14. Optimized geometries of the S_0 and T_1 states of (3,3).

Fig. 15. Energy diagrams of the S_0, S_1, and T_1 states of Et(2,2) and (3,3). Observed values were estimated from the absorption and emission wavelengths. Calculated emission values were obtained by TD-DFT calculations using the optimized geometry of the T_1 state. Calculated Stokes shift values are difference between the observed absorption and calculated emission values.

Fig. 16. Filling models of optimized geometries of Et(2,2) and (3,3).

Fig. 17. Schematic potentials of (3, 3) with crowded phenyl groups and Et(2, 2) with non-crowded phenyl groups.

Fig. 18. Schematic Frank-Condon factors in three different configurations between the ground and excited states: (a) same equilibrium position in the same normal coordinate, (b) different equilibrium position in the same normal coordinate, (c) two potentials located in different normal coordinates.

Figure 1.

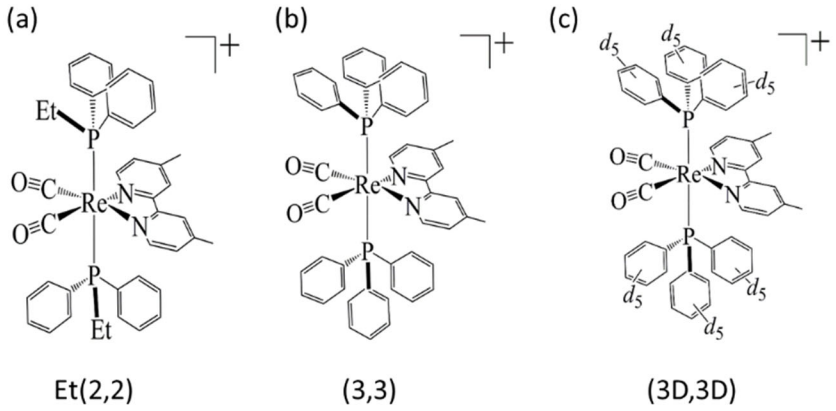

Figure 2.

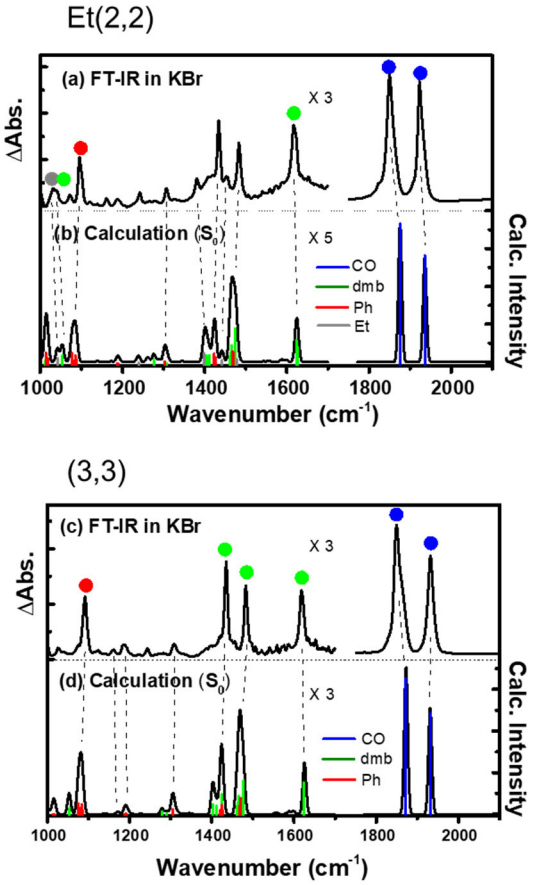
Et(2,2)
(a) FT-IR in KBr
X 3
ΔAbs.
(b) Calculation (S0)
X 5
CO
dmb
Ph
Et
Calc. Intensity
1000
1200
1400
1600
1800
2000
Wavenumber (cm-1)
(3,3)
(c) FT-IR in KBr
X 3
ΔAbs.
(d) Calculation (S0)
X 3
CO
dmb
Ph
Calc. Intensity
1000
1200
1400
1600
1800
2000
Wavenumber (cm-1)

Figure 3.

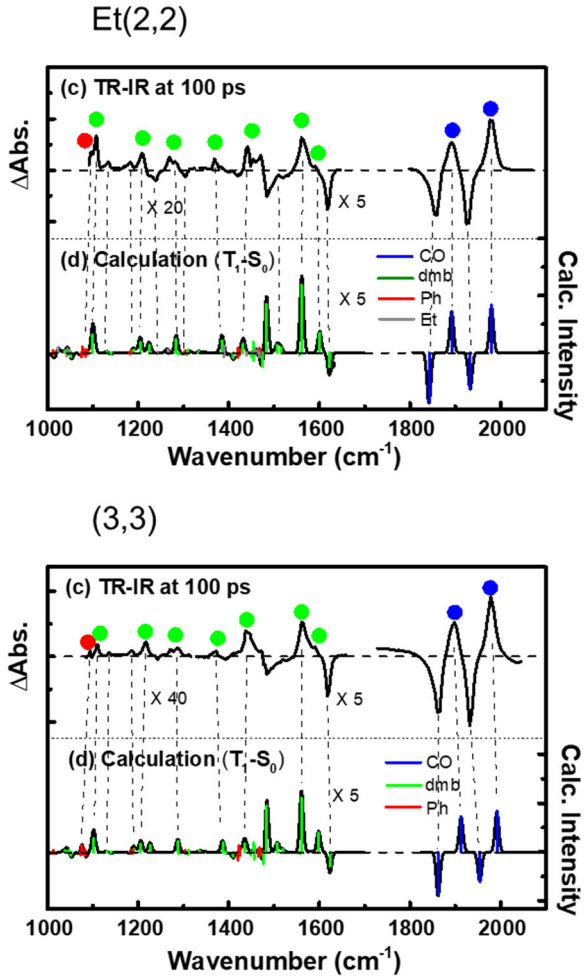
Et(2,2)
(c) TR-IR at 100 ps
ΔAbs.
X 20
X 5
(d) Calculation (T1-S0)
X 5
CO
dmb
Ph
Et
Calc. Intensity
1000
1200
1400
1600
1800
2000
Wavenumber (cm-1)
(3,3)
(c) TR-IR at 100 ps
ΔAbs.
X 40
X 5
(d) Calculation (T1-S0)
X 5
CO
dmb
Ph
Calc. Intensity
1000
1200
1400
1600
1800
2000
Wavenumber (cm-1)

Figure 4.

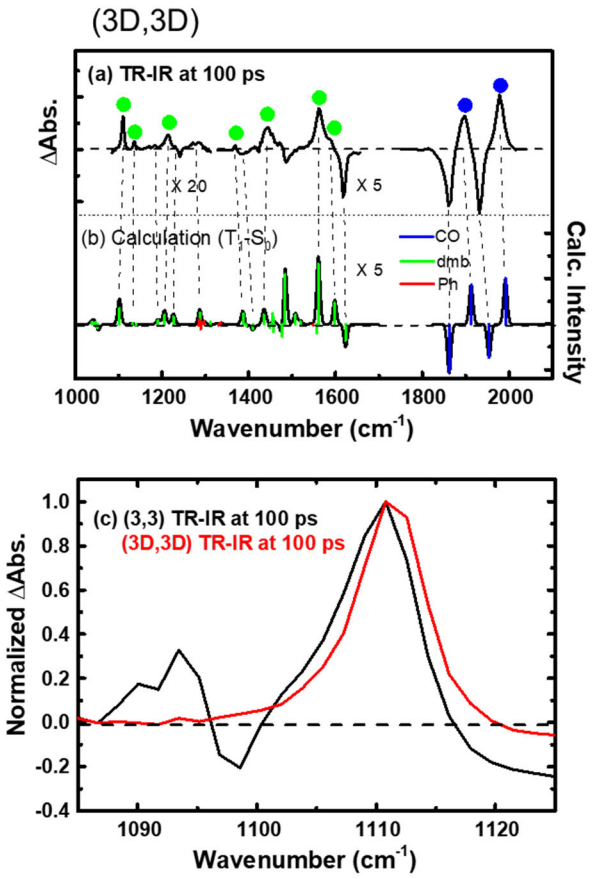
(3D,3D)
(a) TR-IR at 100 ps
ΔAbs.
X 20
X 5
(b) Calculation (T_1-S_0)
CO
dmb
Ph
X 5
Calc. Intensity
1000
1200
1400
1600
1800
2000
Wavenumber (cm^{-1})
(c) (3,3) TR-IR at 100 ps
(3D,3D) TR-IR at 100 ps
Normalized ΔAbs.
1.0
0.8
0.6
0.4
0.2
0.0
-0.2
-0.4
1090
1100
1110
1120
Wavenumber (cm^{-1})

Figure 5.

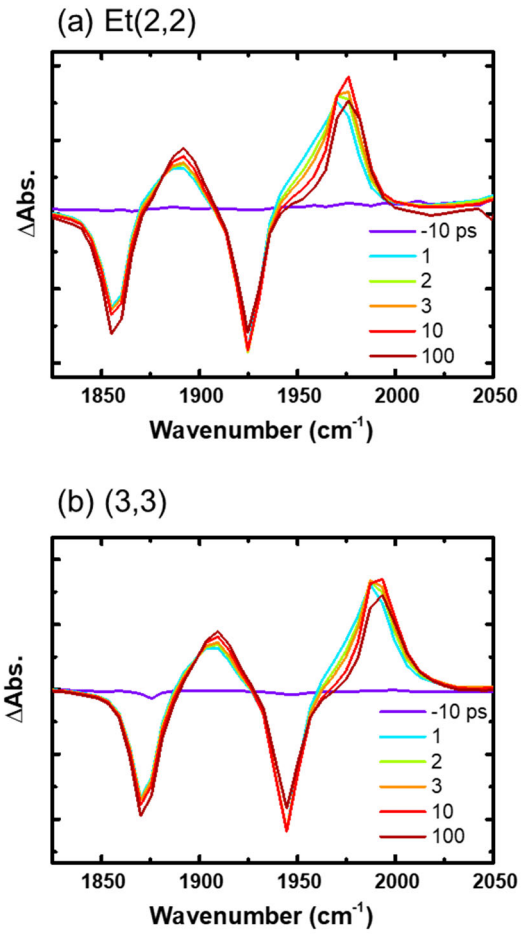
(a) Et(2,2)
ΔAbs.
-10 ps
1
2
3
10
100
1850
1900
1950
2000
2050
Wavenumber (cm-1)
(b) (3,3)
ΔAbs.
-10 ps
1
2
3
10
100
1850
1900
1950
2000
2050
Wavenumber (cm-1)

Figure 6.

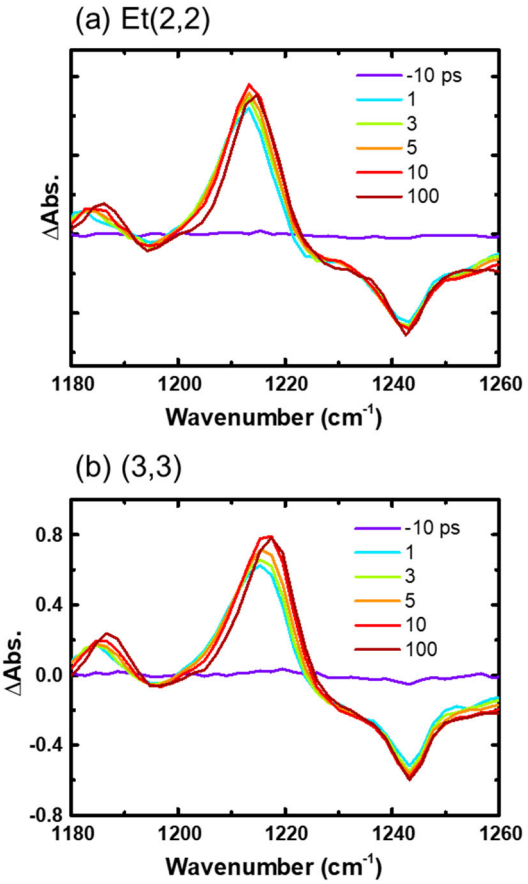
(a) Et(2,2)
-10 ps
1
3
5
10
100
ΔAbs.
1180
1200
1220
1240
1260
Wavenumber (cm-1)
(b) (3,3)
-10 ps
1
3
5
10
100
ΔAbs.
0.8
0.4
0.0
-0.4
-0.8
1180
1200
1220
1240
1260
Wavenumber (cm-1)

Figure 7.

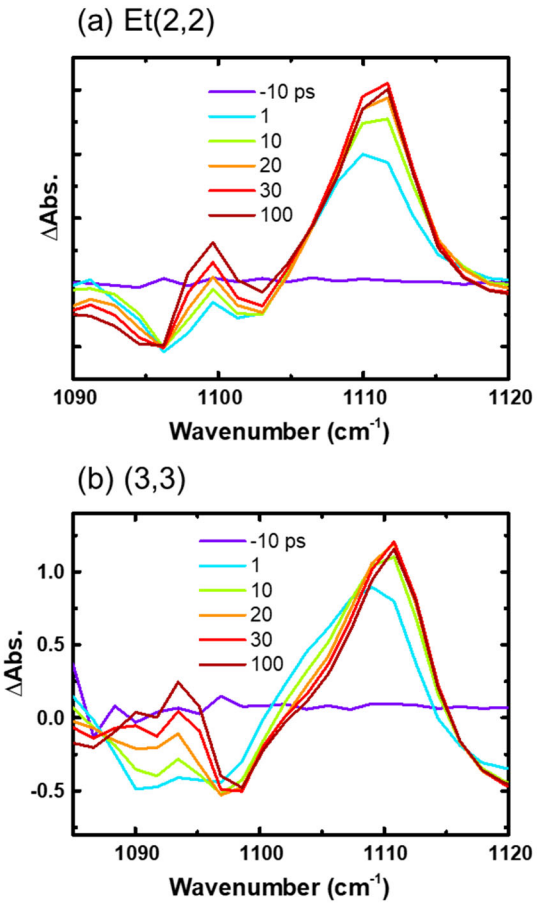
(a) Et(2,2)
-10 ps
1
10
20
30
100
ΔAbs.
1090
1100
1110
1120
Wavenumber (cm-1)
(b) (3,3)
-10 ps
1
10
20
30
100
ΔAbs.
1.0
0.5
0.0
-0.5
1090
1100
1110
1120
Wavenumber (cm-1)

Figure 8.

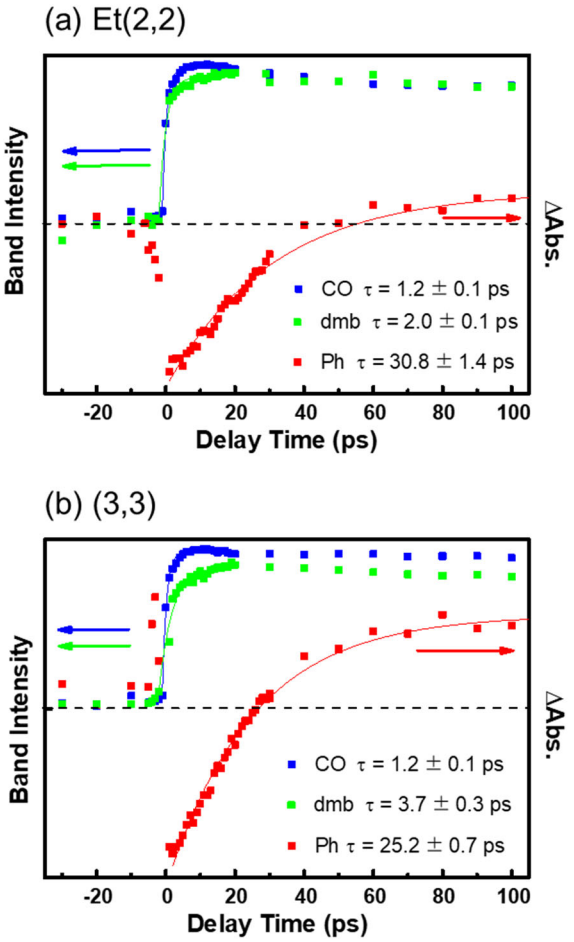
(a) Et(2,2)
Band Intensity
ΔAbs.
CO τ = 1.2 ± 0.1 ps
dmb τ = 2.0 ± 0.1 ps
Ph τ = 30.8 ± 1.4 ps
-20
0
20
40
60
80
100
Delay Time (ps)
(b) (3,3)
Band Intensity
ΔAbs.
CO τ = 1.2 ± 0.1 ps
dmb τ = 3.7 ± 0.3 ps
Ph τ = 25.2 ± 0.7 ps
-20
0
20
40
60
80
100
Delay Time (ps)

Figure 9.

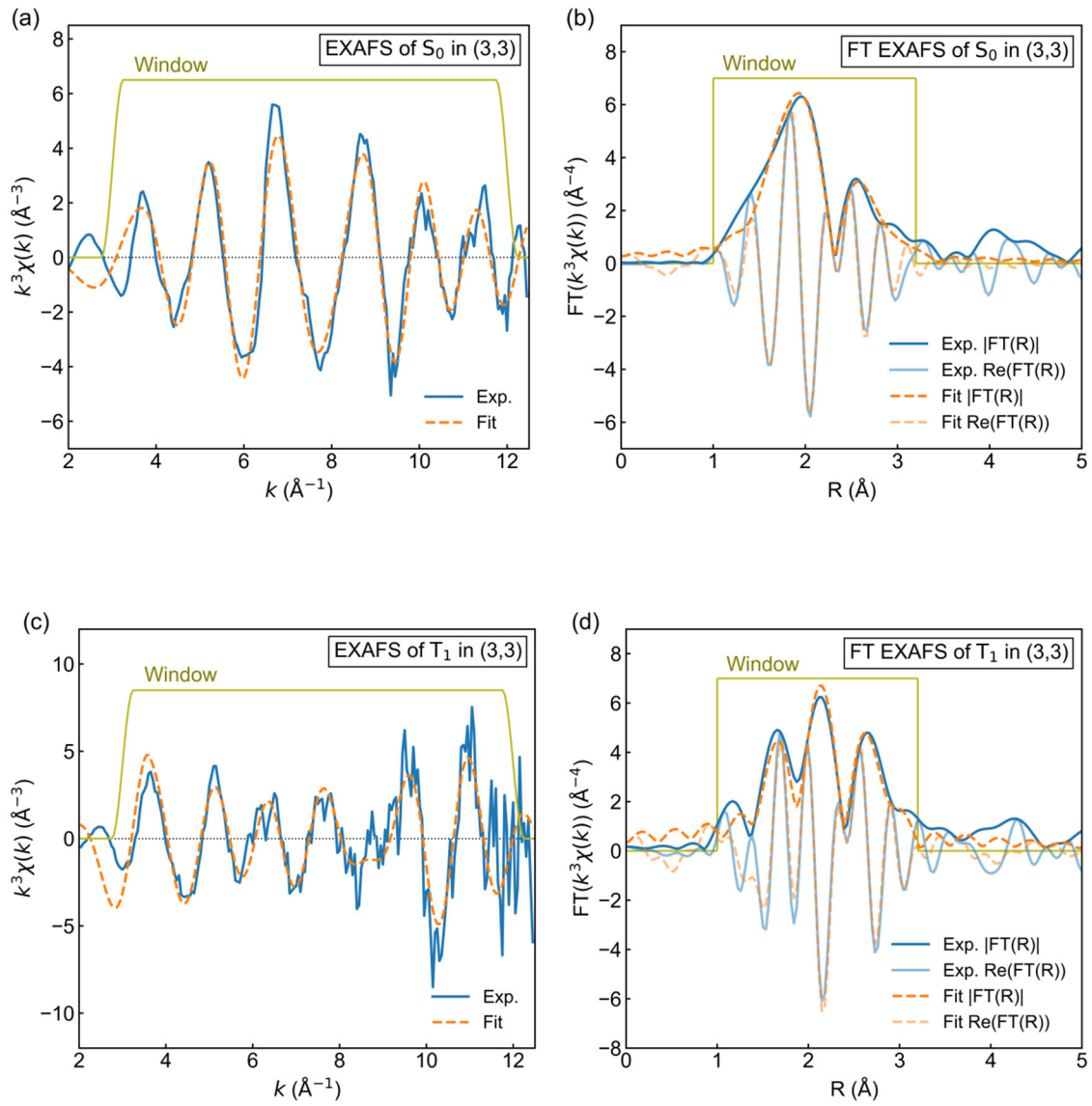
(a)
EXAFS of S_0 in (3,3)
Window
$k^3\chi(k)$ (Å^{-3})
k (Å^{-1})
Exp.
Fit
(b)
FT EXAFS of S_0 in (3,3)
Window
FT($k^3\chi(k)$) (Å^{-4})
R (Å)
Exp. |FT(R)|
Exp. Re(FT(R))
Fit |FT(R)|
Fit Re(FT(R))
(c)
EXAFS of T_1 in (3,3)
Window
$k^3\chi(k)$ (Å^{-3})
k (Å^{-1})
Exp.
Fit
(d)
FT EXAFS of T_1 in (3,3)
Window
FT($k^3\chi(k)$) (Å^{-4})
R (Å)
Exp. |FT(R)|
Exp. Re(FT(R))
Fit |FT(R)|
Fit Re(FT(R))

Figure 10.

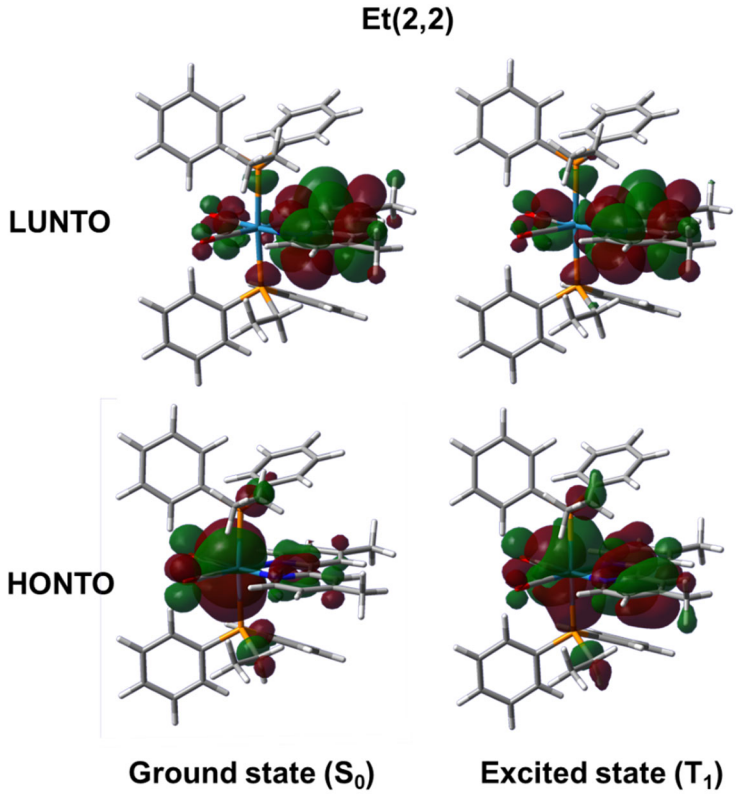

Figure 11.

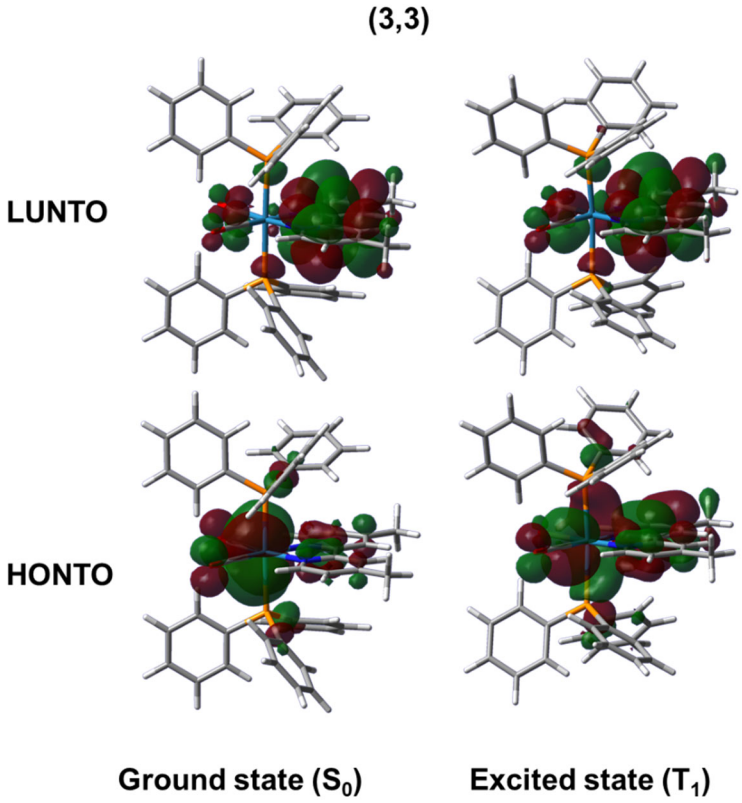

Figure 12.

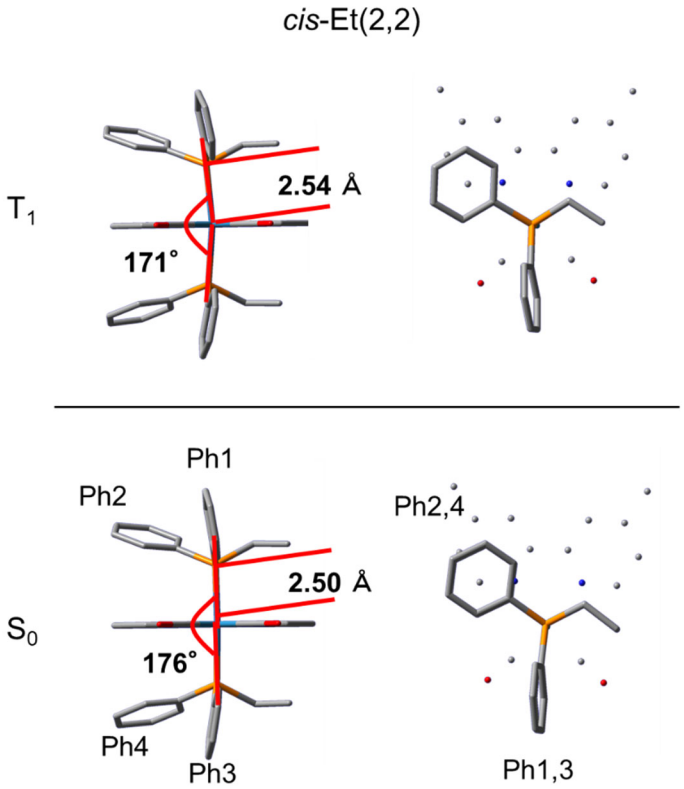

Figure 13.

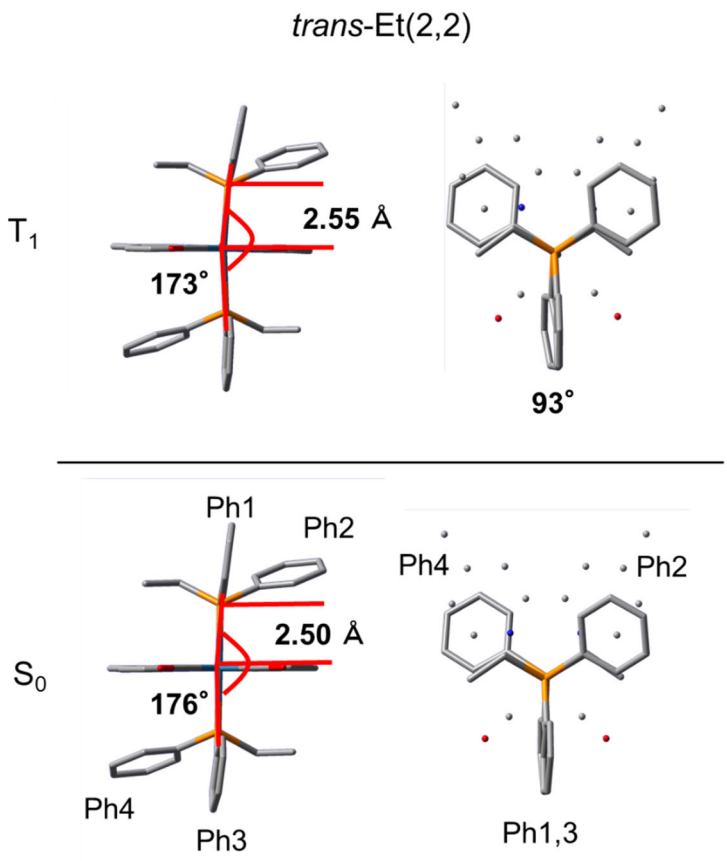
trans-Et(2,2)
T1
2.55 Å
173°
93°
S0
Ph1
Ph2
2.50 Å
176°
Ph4
Ph3
Ph4
Ph2
Ph1,3

Figure 14.

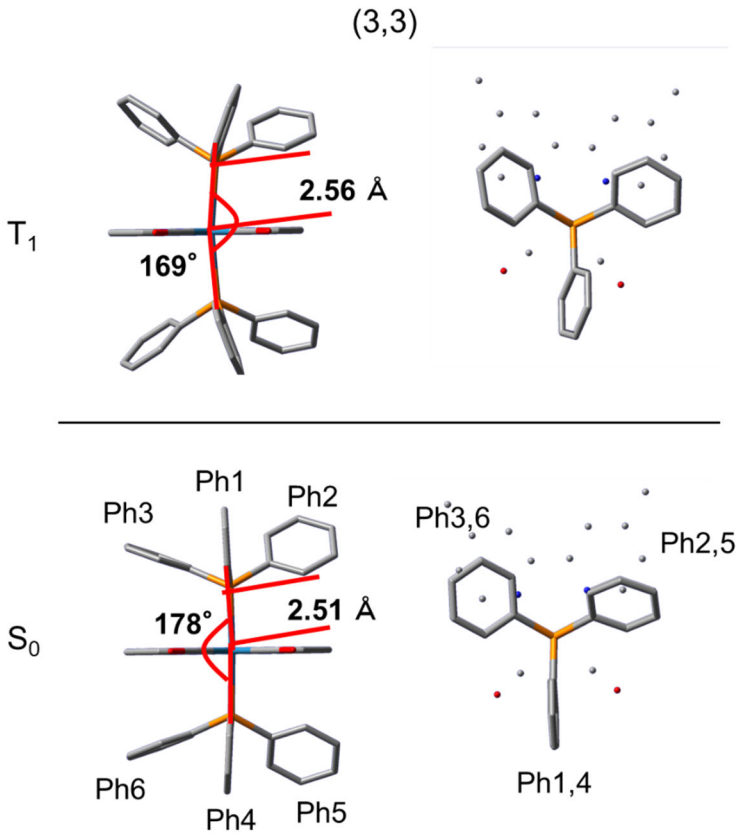
(3,3)
T1
2.56 Å
169°
S0
Ph1
Ph2
Ph3
178°
2.51 Å
Ph6
Ph4
Ph5
Ph3,6
Ph2,5
Ph1,4

Figure 15.

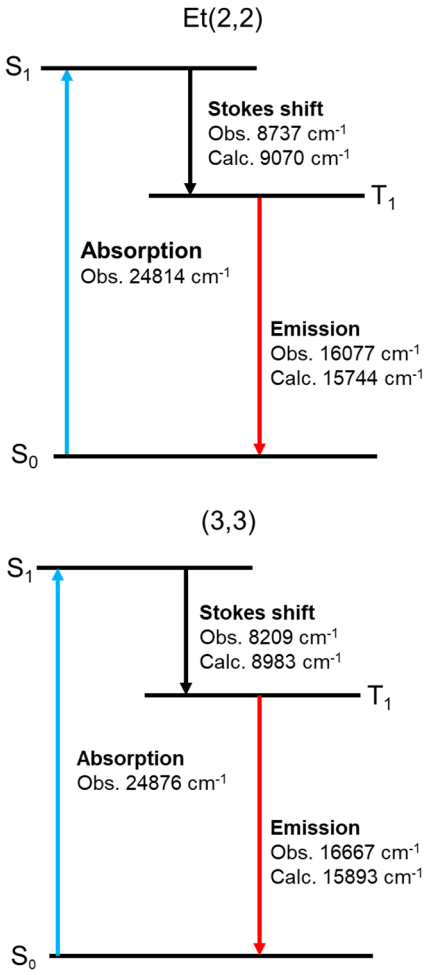
Et(2,2)
S1
Stokes shift
Obs. 8737 cm-1
Calc. 9070 cm-1
T1
Absorption
Obs. 24814 cm-1
Emission
Obs. 16077 cm-1
Calc. 15744 cm-1
S0
(3,3)
S1
Stokes shift
Obs. 8209 cm-1
Calc. 8983 cm-1
T1
Absorption
Obs. 24876 cm-1
Emission
Obs. 16667 cm-1
Calc. 15893 cm-1
S0

Figure 16.

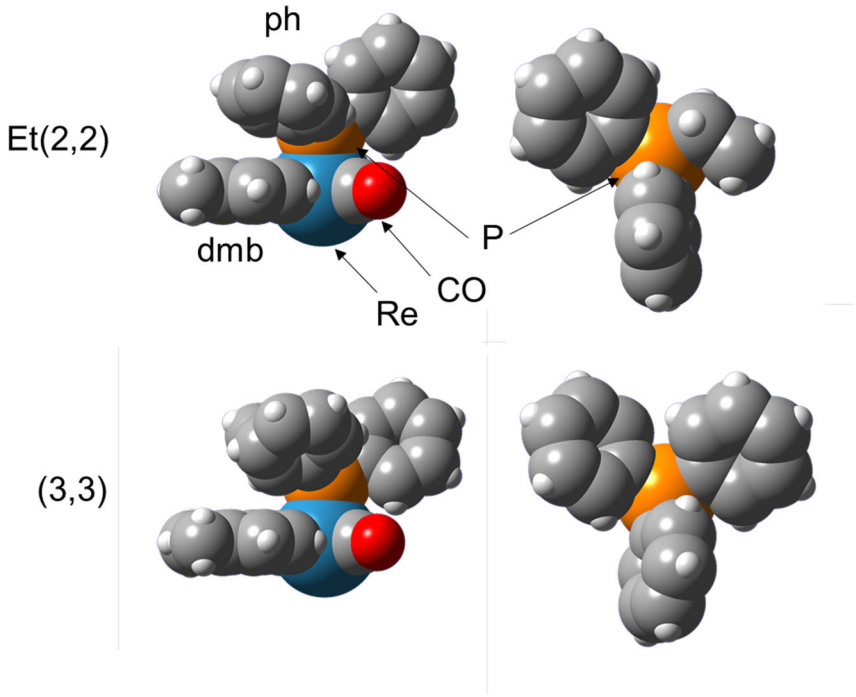

Figure 17.

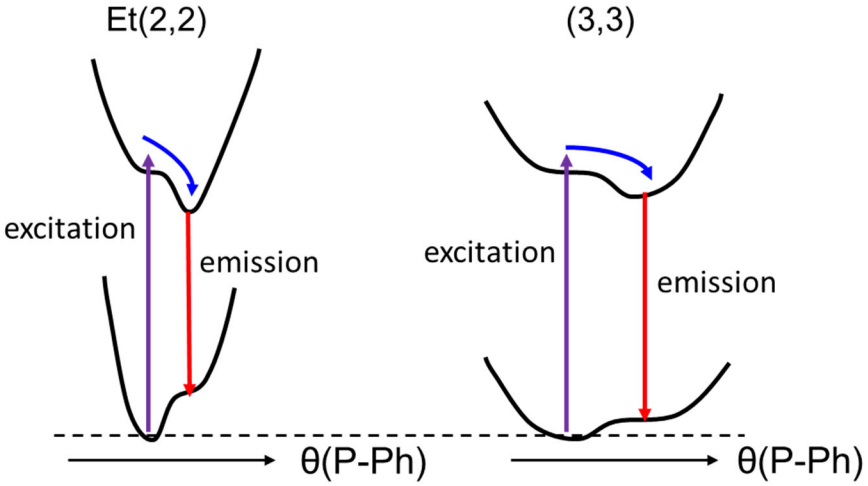
Et(2,2)
excitation
emission
θ(P-Ph)
(3,3)
excitation
emission
θ(P-Ph)

Figure 18.

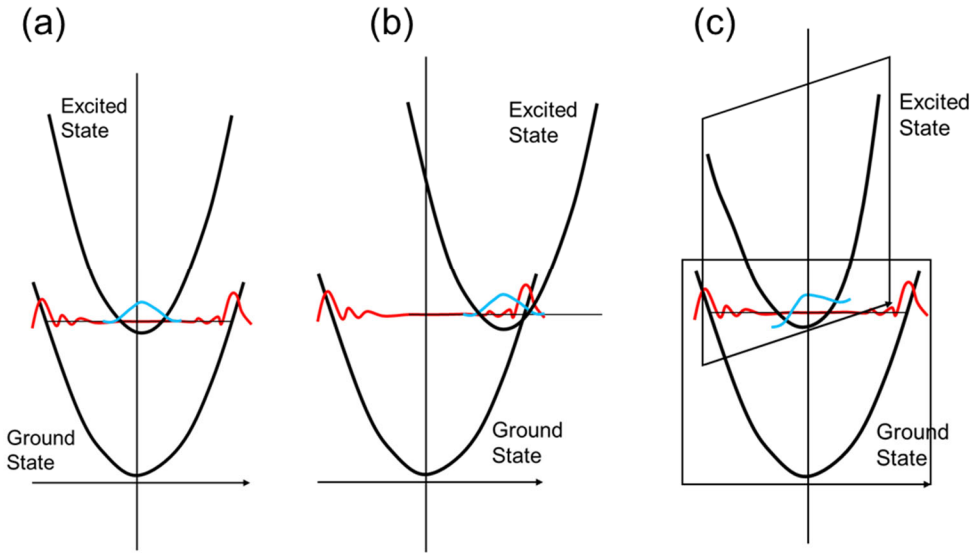
(a)
Excited State
Ground State
(b)
Excited State
Ground State
(c)
Excited State
Ground State

Supporting Information

Determining Excited-State Structures and Photophysical Properties in Phenylphosphine Rhenium(I) Diimine Biscarbonyl Complexes Using Time-Resolved Infrared and X-ray Absorption Spectroscopies

Yuushi Shimoda[1], Kiyoshi Miyata[1], Masataka Funaki[2], Tatsuki Morimoto[3], Shunsuke Nozawa[4,*], Shin-ichi Adachi[4], Osamu Ishitani[2], and Ken Onda[1,*]

[1]Department of Chemistry, Faculty of Science, Kyushu University, Motooka, Nishi-ku, Fukuoka 819-0395, Japan

[2]Department of Chemistry, School of Science, Tokyo Institute of Technology, O-okayama, Meguro-ku, Tokyo 152-8551, Japan

[3]Department of Applied Chemistry, School of Engineering, Tokyo University of Technology, Katakuramachi, Hachioji City, Tokyo 192-0982, Japan.

[4]Photon Factory, Institute of Materials Structure Sciences, High Energy Accelerator Research Organization (KEK), Oho, Tsukuba, Ibaraki 305-0801 Japan

*Corresponding authors: konda@chem.kyushu-univ.jp, noz@post.kek.jp

Figure S1. Typical normal vibrational modes of S_0 in *cis*-E(2,2).

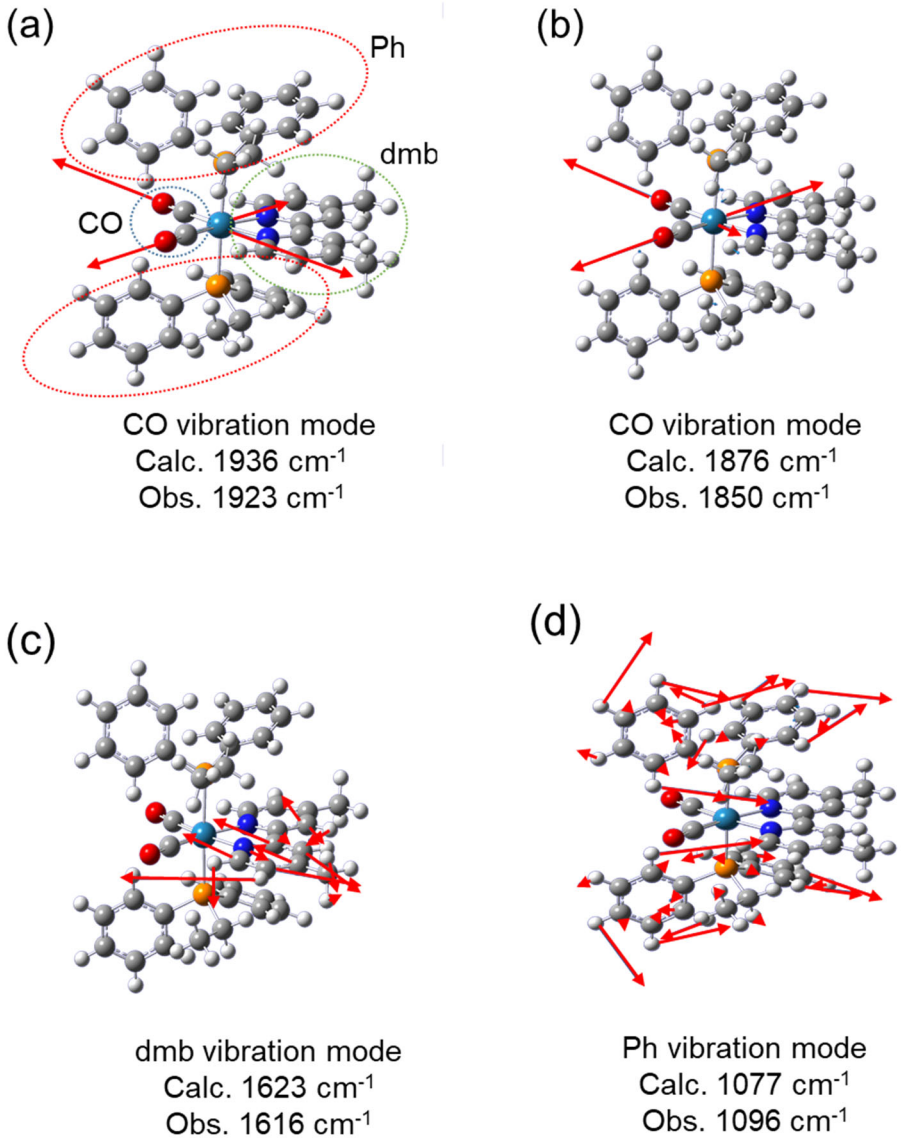

Figure S2. Typical normal vibrational modes of T_1 in *cis*-E(2,2).

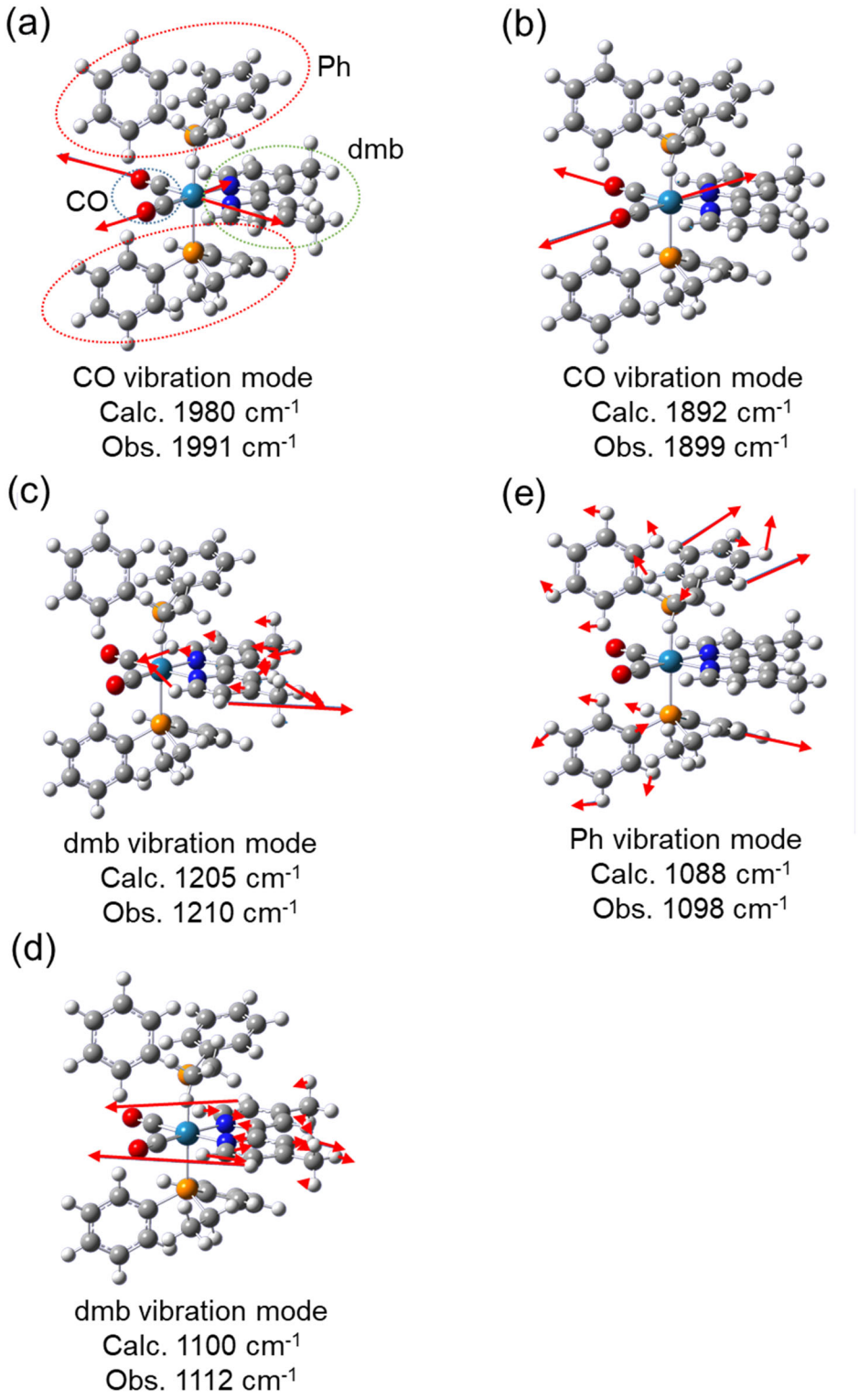

Figure S3. Typical normal vibrational modes of S_0 in (3,3).

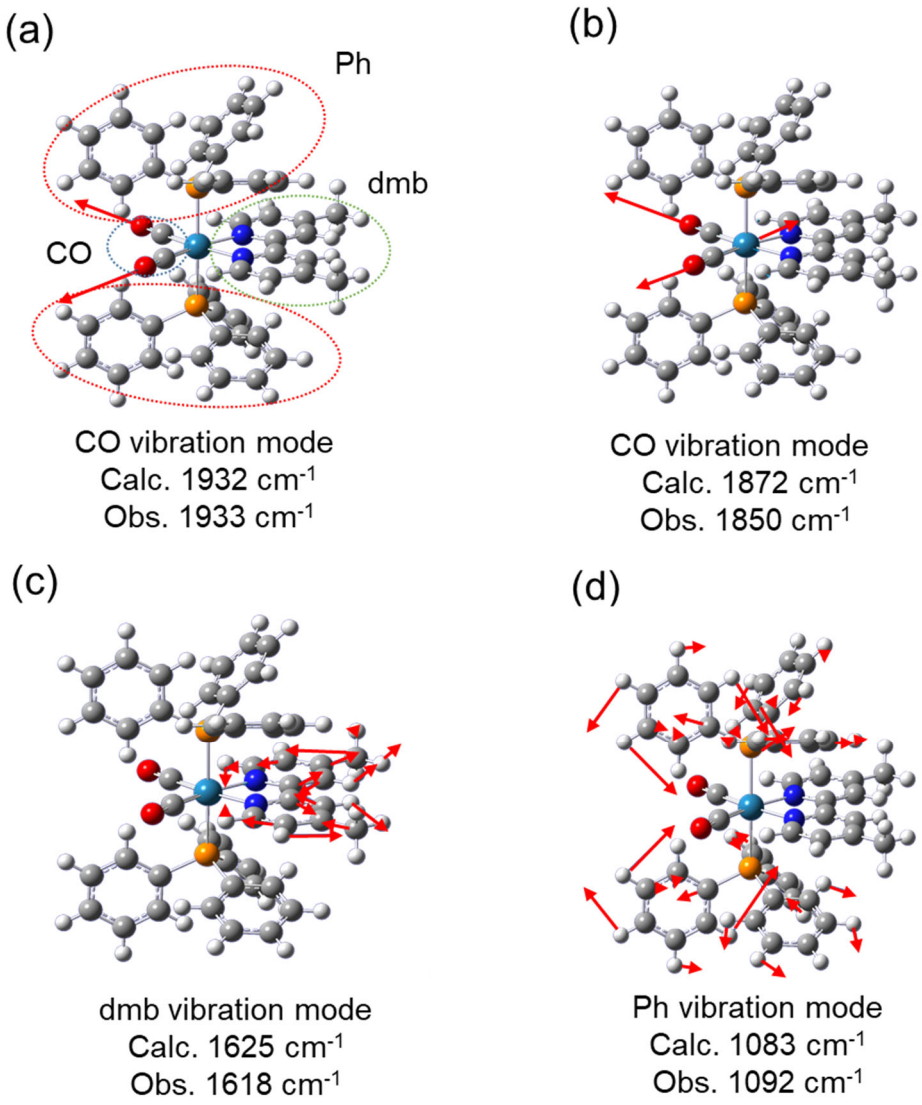

Figure S4. Typical normal vibrational modes of T_1 in (3,3).

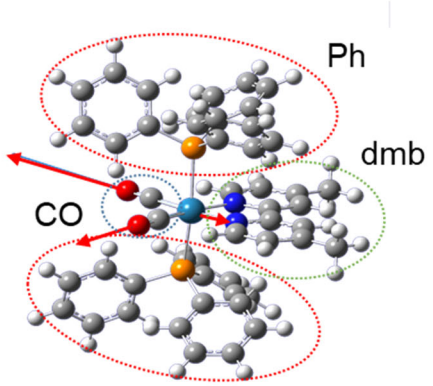

CO vibration mode
Calc. 1974 cm^{-1}
Obs. 1986 cm^{-1}

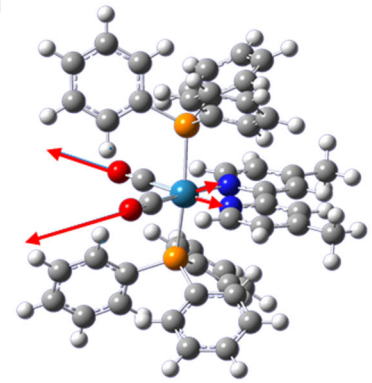

CO vibration mode
Calc. 1894 cm^{-1}
Obs. 1905 cm^{-1}

(c)

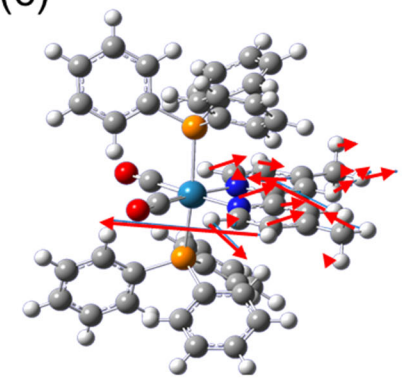

dmb vibration mode
Calc. 1206 cm^{-1}
Obs. 1217 cm^{-1}

(e)

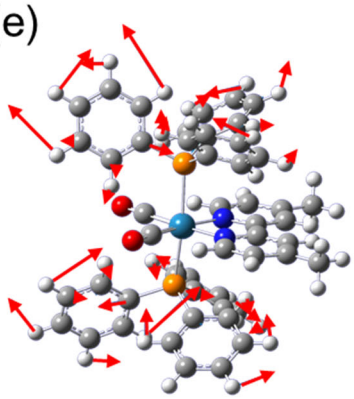

Ph vibration mode
Calc. 1084 cm^{-1}
Obs. 1093 cm^{-1}

(d)

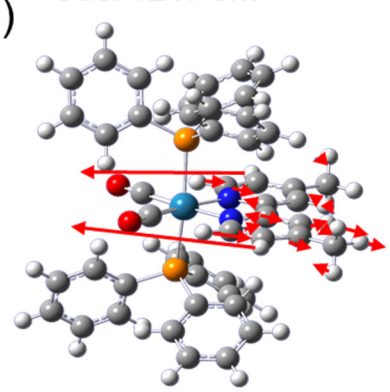

dmb vibration mode
Calc. 1102 cm^{-1}
Obs. 1111 cm^{-1}

Figure S5. Comparison of TR-IR spectra of (3,3) and (3D,3D).

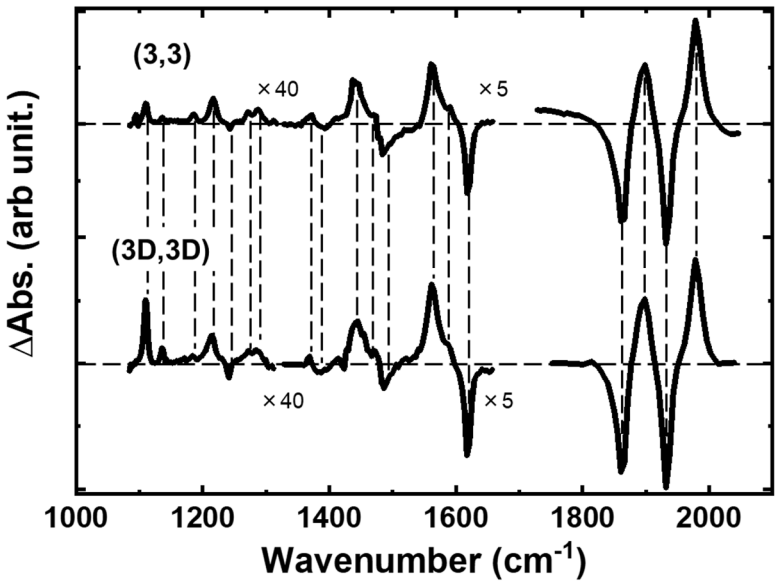

Figure S6. Comparison of observed FT-IR and TR-IR spectra of (a) Et(2,2) with the calculated spectra of the (b) cis- and (c) trans-Et(2,2) geometries.

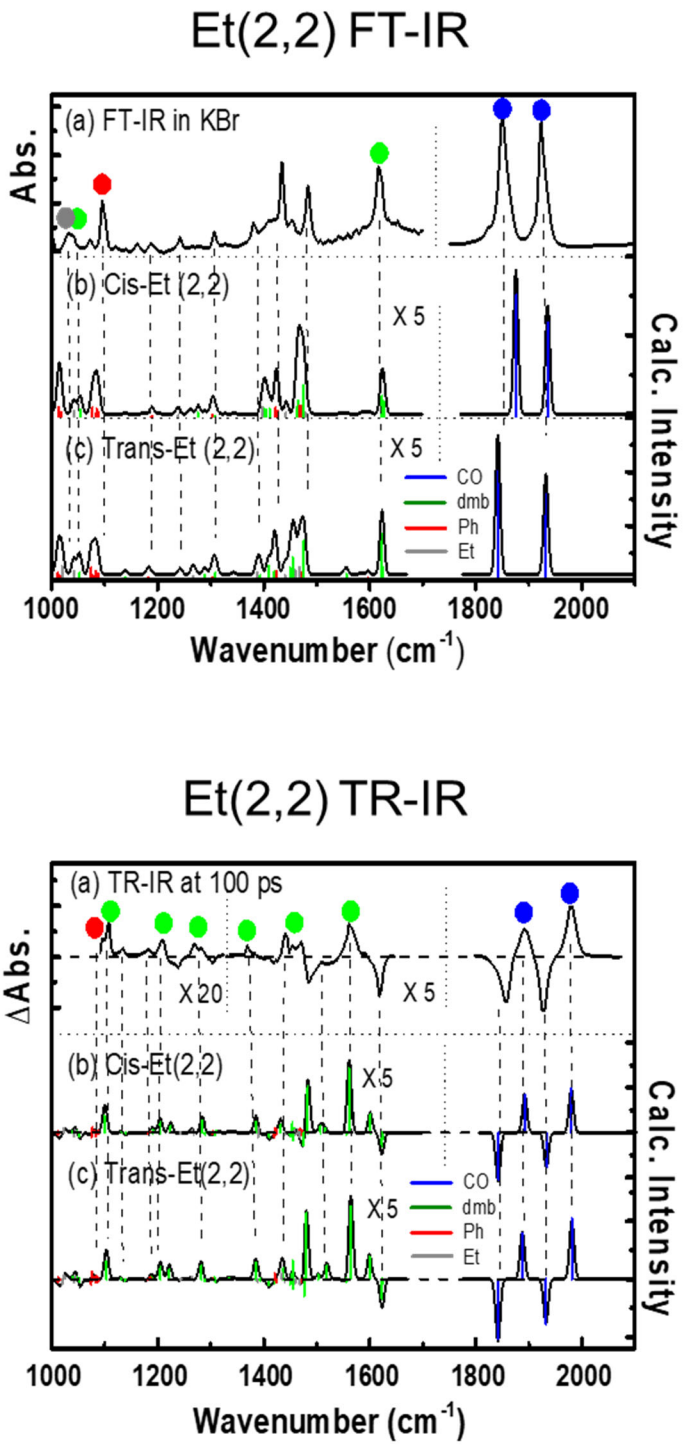

Table S1. Selected bond lengths and dihedral angles in the optimized geometries of S_0 and T_1 in *cis*-Et(2,2). Atom labels are shown in the schematic below.

Bond lengths/ Å	S_0 calc.	T_1 calc.	Difference
Re-C1	1.89	1.96	0.07
Re-C2	1.89	1.90	0.01
Re-P1	2.50	2.54	0.05
Re-P2	2.50	2.54	0.05
Re-N1	2.16	2.14	-0.02
Re-N2	2.16	2.05	-0.10

Angles / °	S_0 calc.	T_1 calc.	Difference
P1-Re-P2	177.6	169.5	**-4.6**
C1-Re-C2	93.0	91.9	-2.0
N1-Re-N2	75.1	77.7	2.8

Dihedral Angles / °	S_0 calc.	T_1 calc.	Difference
Ph1(P2,P1,C3,C4)	170.2	168.2	**-2.0**
Ph2(P2,P1,C5,C6)	95.3	93.7	**-1.6**
Ph3(P1,P2,C7,C8)	-170.2	-168.2	**2.0**
Ph4(P1,P2,C9,C10)	95.3	-93.7	**1.6**

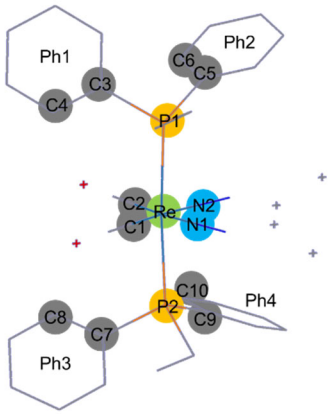

Table S2. Selected bond lengths and dihedral angles in the optimized geometries of S_0 and T_1 in (3,3). Atom labels are shown in the schematic below.

Bond lengths/ Å	S_0 calc.	T_1 calc.	Difference
Re-C1	1.89	1.96	0.07
Re-C2	1.89	1.90	0.01
Re-P1	2.51	2.56	0.05
Re-P2	2.51	2.56	0.05
Re-N1	2.16	2.14	-0.02
Re-N2	2.15	2.05	-0.01

Angles / °	S_0 calc.	T_1 calc.	Difference
P1-Re-P2	177.6	169.5	**-8.1**
C1-Re-C2	93.0	91.9	-1.0
N1-Re-N2	75.1	77.7	2.6

Dihedral Angles / °	S_0 calc.	T_1 calc.	Difference
Ph1(P2,P1,C3,C4)	182.6	156.0	**-26.6**
Ph2(P2,P1,C5,C6)	51.6	67.9	**16.3**
Ph3(P2,P1,C7,C8)	96.0	117.1	**21.1**
Ph4(P1,P2,C9,C10)	177.0	204.0	**27.0**
Ph5(P1,P2,C11,C12)	-51.9	-67.8	**-16.0**
Ph6(P1,P2,C13,C14)	-95.8	-117.1	**-21.3**

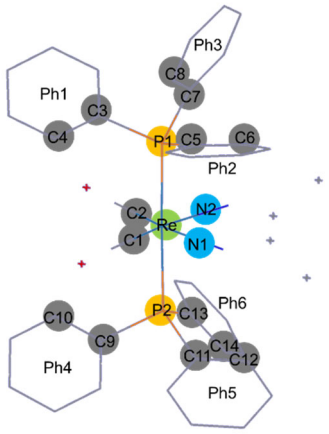

Details of EXAFS Analysis

The wavenumber (k) ranges in the Fourier transformation were 3 to 12 Å^{-1}, as shown in the windows in Figure 14a and 14c. The Fourier transformed EXAFS functions $k^3 \times f(k)$ of the S_0 and T_1 states at 100 ps are shown as lines in Figure 14b and 14d. The curve-fitting analysis was performed in R space using the single scatterings from the first nearest neighbor (NN) (Re-C in CO, Re-N in dmb, and Re-P in PPh_3), the single scatterings from the second NN (Re-C in dmb and Re-O in CO), and the multiple scatterings in dmb and CO. The R range employed in the curve-fitting analysis was ΔR ~1–3.2 Å, as shown in the windows in Figure 14b and 14d. The scattering amplitudes and phase shifts were calculated by the FEFF 6 code [1] from the DFT orientations. Throughout the curve-fitting analysis, the parameters of the coordination numbers were held constant at the same values as the composition formula. For both S_0 and T_1, an energy origin for EXAFS (E_0) was determined to be 10533 eV from the inflection point obtained by the first derivative of the Re-*LIII* absorption edge of the S_0 spectrum. For all scattering paths in S_0 and T_1, the same amplitude reduction factor (S_0^2) and energy shift (ΔE_0) from E_0 were applied. The bond length of each scattering path was expressed by an expansion factor (α) and half path distance ($reff$) from the DFT orientation as $\alpha \times reff$. For the scattering paths from the dmb, CO, and PPh_3 ligands, different α and different mean-square displacements (DMS) (σ^2) were considered as α_{dmb}, α_{CO}, α_P, and σ^2_{dmb}, σ^2_{CO}, σ^2_P. For the DMS in multi-scattering paths, σ^2_{multi} was used as the fitting parameter. Data analysis was performed by the Larch software package [2] using a Python library.

In regards to S_0, a normal EXAFS analysis was performed using the above parameters as shown in Figure 14a and 14b. The results are shown in Table S3.

The T_1 EXAFS spectrum $f(k,\tau)_{T_1}$ was obtained by the expression

$$f(k,\tau)_{T_1} = F(\tau)\Delta f(k,\tau) + f(k)_{S_0} \quad (1)$$

where $F(\tau)$ is the scale factor at the delay time τ, $f(k)_{T_1}$ is the absorption spectrum of the S_0 ground state, and $\Delta f(k,\tau)$ is the difference absorption spectrum at τ. To obtain $F(\tau)$ at τ = 100 ps, the minimum R-factor, which indicates the closeness-of-fit [3], was explored to give the values of $F(\tau)$ and ΔE_0 [4,5]. From the mapping of R-factors for $F(\tau)$ and ΔE_0 shown in Figure S7, the minimum R-factor was obtained at $F(\tau)$ = 0.014 and ΔE_0 = 13 eV. In this case, the fraction of T_1 at τ = 100 ps was estimated to be 1.4%. The EXAFS spectrum of the T_1 state shown in Figure 14c was derived by eq. (1) with $F(\tau)$ = 0.014. The EXAFS analysis for T_1 was performed using the same parameters in S_0. Table S3 shows the fitting results for T_1. Although the valence of S_0 is Re(I), the valence of T_1 is Re(II) because it is a transient charge transfer state. Therefore, in the EXAFS fitting result, the ΔE_0 of T_1 is larger than that of S_0 because of the effect of chemical shift.

Figure S7. R-factor mapping for F(τ) and ΔE_0 in the EXAFS analysis of T_1 in (3,3).

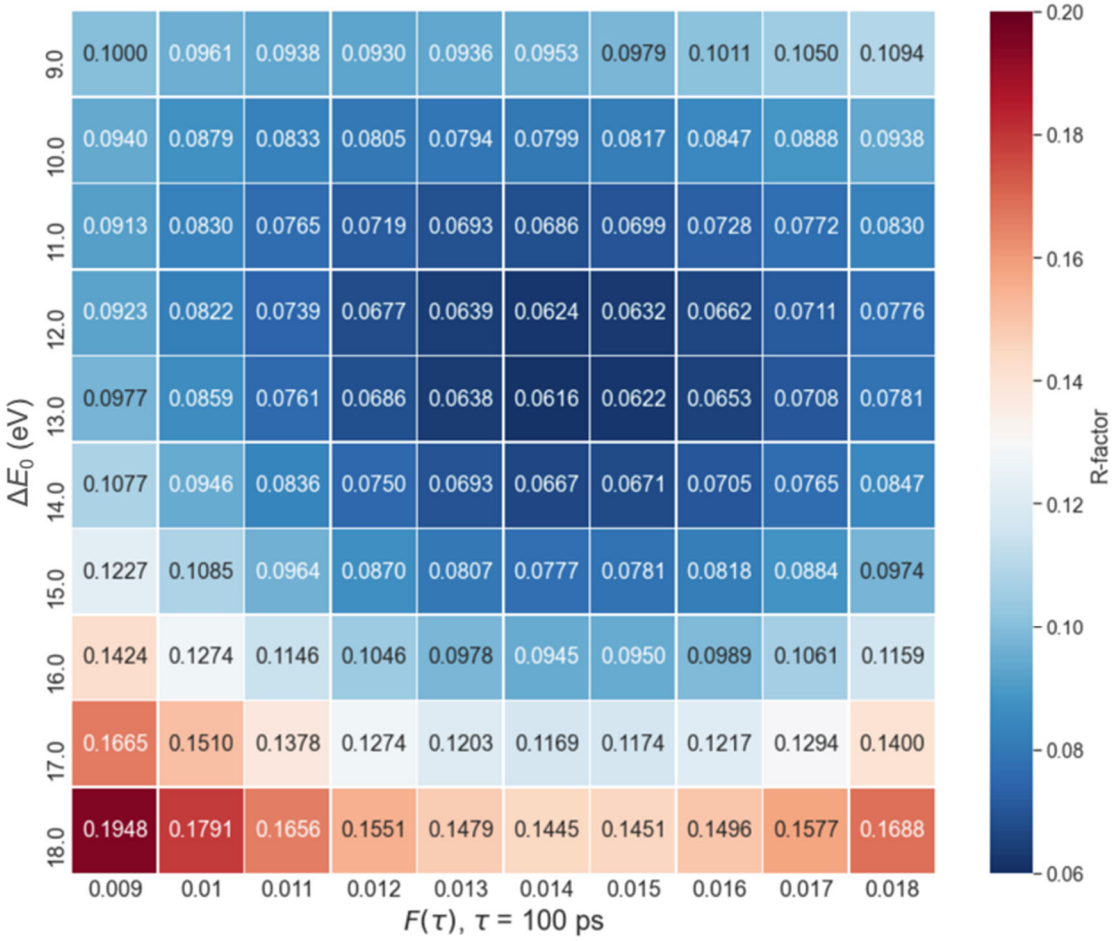

Table S3. Fitting results from the EXAFS analysis of S_0 and T_1 in (3,3).

	S_0	T_1
R-factor	0.029	0.061
S_0^2	1.0(3)	1.4(5)
ΔE_0	5.0(27)	12.6(21)
α_{dmb}	-0.012(13)	-0.013(7)
α_{CO}	-0.013(6)	-0.003(6)
α_P	-0.039(7)	-0.005(6)
σ_{dmb}^2	0.004(4)	0.001(1)
σ_{CO}^2	0.006(3)	0.015(13)
σ_P^2	0.004(2)	0.005(3)
σ_{multi}^2	0.004(2)	0.003(3)

References

[1] Zabinsky, S. I.; Rehr, J. J.; Ankudinov, A.; Albers, R. C.; Eller, M. J., Multiple-scattering calculations of x-ray-absorption spectra. *Phys Rev B Condens Matter* **1995,** *52* (4), 2995-3009.

[2] Newville, M. In *Larch: an analysis package for XAFS and related spectroscopies*, 2013; p 012007.

[3] Calvin, S., *XAFS for Everyone*. CRC press: 2013.

[4] Gawelda, W.; Pham, V. T., RM van der Veen, D. Grolimund, R. Abela, M. Chergui, C. Bressler. *J. Chem. Phys* **2009,** *130*, 124520.

[5] Sato, T.; Nozawa, S.; Tomita, A.; Hoshino, M.; Koshihara, S.; Fujii, H.; Adachi, S., Coordination and electronic structure of ruthenium (II)-tris-2, 2′ -bipyridine in the triplet metal-to-ligand charge-transfer excited state observed by picosecond time-resolved Ru K-edge XAFS. *The Journal of Physical Chemistry C* **2012,** *116* (27), 14232-14236.